Sub-20nm Substrate Patterning Using A Self-Assembled Nanocrystal Template

by

Ryan C. Tabone

B.S., Electrical Engineering and Computer Engineering (2003)
Johns Hopkins University

Submitted to the Department of Electrical Engineering and Computer Science
in partial fulfillment of the requirements for the degree of

MASTER OF SCIENCE IN ELECTRICAL ENGINEERING

at the

MASSACHUSETTS INSTITUTE OF TECHNOLOGY

June 2005

Signature of Author ....
Department of Electrical Engineering and Computer Science
May 10, 2005

Certified by ....
Vladimir Bulović
Associate Professor, KDD Career Development Chair
Thesis Supervisor

Accepted by ....
Arthur C. Smith
Chairman, Committee on Graduate Students
Department of Electrical Engineering and Computer Science

Sub-20nm Substrate Patterning Using A Self-Assembled Nanocrystal Template

by

Ryan C. Tabone

Submitted to the Department of Electrical Engineering and Computer Science
on May 10, 2005, in partial fulfillment of the
requirements for the degree of
MASTER OF SCIENCE IN ELECTRICAL ENGINEERING

Abstract

A hexagonally close-packed monolayer of lead selenide quantum dots is presented as a template for patterning with a tunable resolution from 2 to 20nm. Spin-casting and micro-contact printing are resolved as methods of forming and depositing these monolayers of quantum dots through self-assembly. Four methods of templated patterning - shadowmasking, lift-off, selective ablation & nano-imprinting - using the quantum dot self-assembled monolayer are proposed and explored. The nano-imprinting technique is used to produce the smallest pattern in anodized alumina to date. The use of this nano-patterned anodized alumina as an etch mask is discussed as a means of patterning substrates within the 2 to 20nm range. The physics behind the possible modification of silicon's electronic band gap due to our nano-patterning is also presented.

Thesis Supervisor: Vladimir Bulović
Title: Associate Professor, KDD Career Development Chair

Acknowledgments

It is very difficult to write an acknowledgments section. Why? Because you either want to thank everyone you've ever met in your life, or you brain freeze after spending a month writing one paper which is supposed to prove that you did, in fact, learn and achieve *something* in two years. While there are many people that have helped me get to this point in my life, I'm going to scratch off the "I'd like to thank the academy" line and try and limit this section to people who've helped me on the path to this immediate thesis. It seems that's the point after all.

I would like to thank...

- The Microelectronics Advanced Research Corporation (MARCO) Materials, Structures and Devices (MSD) Focus Center, for funding my research.
- Hank Smith, for having enough faith in me to support my initial time at MIT.
- Everyone in the NanoStructures Laboratory, for being very welcoming; especially Mike Walsh and Jim Daley, who were kind enough to walk me through every tool and process step I needed to know.
- Michelle Moniz, for proofreading my thesis and making sure the grammar was as perfect as it could be for an engineer.
- Eric Mattson - my roommate, for suffering through Quantum's "intuition" with me, for making as much fun of anything & everything as I did and for always giving me a reason to have a beer.
- Moungi Bawendi, for allowing me to use his lab's high quality quantum dots, which are the very foundation of my work.
- Jonathan Steckel, for supplying amazing QDs and ridiculous humor - both very much needed.
- Every member of the Laboratory of Organic Optics and Electronics. They have made my last year and half at MIT fun and inspiring. I couldn't ask for a better group of people to work with and wish them all the best of success.

- Alexi Arango, for teaching me LaTeX as a means of writing my thesis - even when I was ready to throw my computer through the window.

- Conor Madigan, for helping me with (read: writing and explaining) the theory behind my work.

- John Kymissis, for having the patience to be the "go-to guy" for any problem I had, for parylene-C-ing every PDMS stamp I made and for helping me to revise this thesis.

- Seth Coe-Sullivan, for leading me by the hand in my first few months in the LOOE group and for providing valuable insight throughout my project.

- Vladimir Bulović, for allowing me to join his very intellectual, fun and loving research group. Having a colleague rather than a boss has made me look forward to work everyday - whether I came in at 8AM or at Noon (which rarely happened, honest). He has been always encouraging, never judgmental and unexplainably happy. I think he seriously needs to consider becoming a motivational speaker. Despite all his achievements and accolades, Vladimir is one of the most humble people I ever met. He has definitely influenced how I see life, and for that I can not thank him enough.

- Jonathan Tabone and Lauren Barris - my brother and sister, for being there whenever I need them. Always a phone call away, no one else can make me laugh as hard or feel as much at home.

- Charles and Doreen Tabone - my parents, for everything. They have the biggest hearts in the world; I am so thankful to have parents who love and support so unconditionally. They have been there for me no matter where I went and no matter what I did. The more facts I learn, people I meet and places I see, the more I realize how amazing and special both of my parents are. They have allowed me to be who I now am. I could not ask for better parents and I love them with all my heart.

Contents

List of Figures

Chapter 1

Introduction

1.1 History

From his inception, man has been fascinated with producing permanent images. To this day, archaeologists still unearth stone, wood and bone carvings dating back thousands of years. The Sumerians are claimed to be the first to transfer an image from one medium to another about 3000 years ago. They achieved this by pressing engraved stone images into clay. One thousand years later, the Chinese are thought to have first produced prints by rubbing. A major achievement was next made in 1440, when Johanes Gutenburg produced the movable-type printing press. By 1446, metals plates were used for printing. In the 16th century, artisans, including the famous Albrecht Dürer, began etching metal plates with acid. By the end of the 18th century, Alois Senenfelder had invented a crude form of lithography as a cheaper method of printmaking [1].

Once the first transistor was made in 1947 by William Shockley, there was a great push to develop those past patterning techniques to fabricate microelectronic devices. This led to the production of the integrated circuit by Jack Kilby in 1958. Since that time, scientists have been developing techniques to produce cheaper, smaller and more power efficient electronics [2]. Nonetheless, revisions of the ancient methods of image transfer listed are still used in the complex patterning of today - some of which are even used in this thesis work!

1.2 Modern Microelectronic Fabrication Techniques

For our discussion, techniques to produce very small features in substrates can be categorized into four means of writing: electric or magnetic fields, focused beams of energized particles, rigid stylii and 'bottom-up' assembly of molecules [3].

1.2.1 Optical Lithography

In 1965, Gordon Moore of Intel made a supposition that the number of transistors on a die would double every year. For that technological feat to occur, major advancements in our ability to produce high resolution patterns were needed. Over the past thirty years, optical lithography has been the tool that has allowed the electronics community to follow the resolution doubling prediction which became known as Moore's Law [4].

Optical lithography uses light, an electromagnetic wave, to generate a pattern in a photosensitive material. Portions of photosensitive material, usually a cocktail of organic polymers, are exposed to light and then developed in a chemical reactant. During the development step, exposed portions either remain or are dissolved, dependent on the type of photosensitive material used. The portions that remain will serve as an etching mask for the underlying substrate. Modern lithography uses very small wavelength light, demagnifying lenses and even media with different indices of refraction to generate masks with a 50nm resolution [3].

In standard optical lithography, the wavelength of light used to expose the photosensitive material limits the resolution of the mask generated. In another form of optical lithography known as contact lithography, a masking pattern is pressed against the surface of the photoresist material. Since there are no lenses needed to demagnify the light, wavelength is not a factor. Thus contact lithography has no known limit as to how small a feature can be made. Contact lithography's caveat is that it is a one-to-one transfer of images; it is thus limited by a requirement for a master pattern which *already* has high resolution features.

In the present day, it has become extremely difficult to use optical lithography to breach the 50nm resolution barrier. Demagnification of patterns and different index of refraction materials are already being pushed to their limits. Research is being conducted on using higher energy, and thus smaller wavelength, light, but these higher energy waves are readily absorbed by normally 'transparent' materials [5]. Therefore, to continue the trend predicted by Moore's Law, other methods of patterning needed to be explored.

1.2.2 Focused Beam Lithography

Focused streams of energetic particles, such as photons, ions or electrons, are also used to create patterns. Laser beams have been used to write patterns by ablating materials both to be removed from [6] and deposited onto [7] a substrate. They have also been used to cross-link polymers, borrowing from the essential methods of optical lithography. Focused ion beams use high velocity and relatively high mass particles to either dope materials with the ion or to "ion mill" material from a surface [8, 9].

The most developed and most utilized version of focused beam lithography is election beam (e-beam) lithography. E-beam lithography uses a focused stream of electrons to modify a chemical resist, typically poly(methyl methacrylate) (PMMA) [3]. While this technique has been shown to achieve features as small as 10nm, it is currently limited to producing periodic structures on the order of 30nm [10] - due to backscattering of electrons from collisions with atoms in the substrate. Although this is a very high resolution technique, pattern production can take hours or days depending on complexity and ultimate size. Consequently, focused beam lithography is not the desired patterning technique for rapidly producing periodic high resolution features.

1.2.3 Stylus Writing

Rigid styli and tips are also used to make patterns on substrates. Styli can deposit ink on a substrate as well as directly engrave patterns in a process known as micromachining [3]. Electrostatic forces in conjunction with ultrasharp tips, such as those used in scanning tunneling microscopy (STM) and atomic force microscopy (AFM), have even been used to arrange individual atoms [11]. Clearly, this is the ultimate resolution attainable. Nonetheless, just as in the case of e-beam lithography, the process is extremely slow.

1.2.4 The Bottom-Up Approach

All the techniques described above are classified as top-down approaches to patterning. This is because all those techniques create smaller features from a larger "bulk" substrate. Bottom-up methods also exist, through which patterns are made from a large assembly of individual atoms and molecules [12]. Assembly can refer to a covalent or non-covalent bonding of atoms as well as a self-assembly of molecules on a substrate [13]. Using molecular construction, the bottom-up approach can be used to pattern up to a 2nm resolution. The self-assembly method can arrange particles of any size through various methods of arrangement. One of the points of the thesis is to show the power of one form of self-assembly as a basis of patterning.

1.3 Motivation

From the methods discussed in the previous section, it is apparent that the electronics world lacks the ability to pattern periodic structures in the range between 2 and 20nm. This is the motivation for the work outlined in this paper. First, let us discuss why 2 to 20nm periodic structures are important to create, besides for putting another notch in the belt of humankind's achievements.

As previously addressed, the capacity to create structures below the current 50nm optical lithography threshold would enable the electronics world to fit more features on a die. Patterning into the realm of a few nanometers takes us beyond just fitting more components on a wafer, though. It also allows us to utilize and modify features of a substrate governed by quantum mechanics. Possible outcomes from the production of 2 to 20nm periodic structures are mobility enhancement and modified electrical properties of a substrate [14, 15, 16]. In addition, these structures may grant the ability to produce redundant points of charge storage for memories, to create luminescent silicon [17] and to extract excitons more efficiently from organic devices. Hexagonally close-packed silicon nanostructures may also serve as the foundation from which quantum computing grows [18].

It is apparent that there are a number of uses for these 2 to 20nm periodic structures. One further potential is to use these nanocrystal monolayers as a template for generating a 2 to 20nm pattern in any substrate. This thesis focuses on developing a methodology which fulfills that very potential.

1.4 Quantum Dot Nanocrystals

Quantum Dots (QDs) are nanometer-sized semiconductor crystals which can either be fabricated epitaxially [19] or in a colloidal solution [20]. QDs have been shown to demonstrate unique electrical [21], luminescent [22, 23] and energy transfer properties [24], which have been studied and utilized in numerous devices. For the purpose of our work, QDs are interesting due to the ability of chemists to fabricate a large number of QDs in solution with precise size control and distribution [20]. In addition, it has been shown that monodisperse QDs can quickly be organized into a hexagonally close-packed monolayer [25].

For the exact synthesis chemistry, please refer to publications of the Bawendi group at MIT [20, 23, 24]. While the exact synthesis of QDs is not necessary for this thesis, a few details need to be known by the reader. These semiconductor crystals, which can be fabricated anywhere between 2 and 20nm in size, are surrounded by an organic cap. The organic type and size varies on the semiconductor crystal fabricated and the type of chemistry used to fabricate it. The QDs discussed in this thesis are primarily lead selenide (PbSe) nanocrystals with oleic acid caps.[1]

---

[1] The author found the following facts interesting and thought it may give the lay reader some perspective on the quantum dots used: The quantum dots that are being manipulated are on the same size scale as a few DNA strands. Also, oleic acid, the organic QD cap, is a monounsaturated fat found in many foods and oils, including olive oil. It has even been claimed to be a cancer-fighting agent [26].

1.5 Device Concept

Our goal is to provide a means of rapid patterning which fills the resolution gap set by modern fabrication techniques. Specifically, we look to fabricate a close-packed periodic structure in any substrate with feature size that can be accurately and precisely tuned to any dimension between 2 and 20 nanometers. In addition, we aim to design a process which can produce this structure over large areas in a relatively short period of time. While processes exist that can fabricate structures near or barely within our 2 to 20nm range, the structures are either not reliably monodisperse, small in feature size while large in inter-feature spacing, or take an extraordinarily long time to fabricate.

The solution rests squarely on our idea to combine what is most advantageous in top-down and bottom-up patterning. Contact lithography is able to reproduce any feature present in a master pattern. However, the need for a master pattern limits the functionality of contact lithography since the lithography world does not have the means of reliably mass-producing 2 to 20nm patterns. It is here that we turn to the bottom-up approach. As discussed in Section 1.4, chemists are able to synthesize nanocrystals both accurately and precisely in a range of 2 to 20nm. These nanocrystals, in turn, can be organized into a hexagonally close-packed structure.

We thus employ a self-assembled hexagonally close-packed colloidal quantum dot monolayer as a template for patterning. By using a QD self-assembled monolayer (SAM), we are able to control the feature size through chemical synthesis. We also choose to use a QD SAM as it can be quickly produced on nearly any substrate. The substrate used to demonstrate results in this thesis is silicon, the foundation of semiconductor technology.

1.6 Structure of Thesis

In Chapter 2, we begin with a brief overview of the physics resulting from 2 to 20nm periodic structures. A basic description of the tools used for sample analysis are given in Chapter 3. Chapters 4 & 5 describe the spin casting and QD micro-contact printing processes. These two QD self-assembled monolayer formation processes are the foundation for the patterning methods detailed in Chapters 6, 7, 8 & 9. These four chapters each discuss the reasoning behind each method, a process description, a presentation of results and a discussion and conclusion based on these results. In Chapter 10, we discuss the impact of this thesis work upon the scientific community. Lastly, Chapter 11 summarizes the conclusions from this thesis work and proposes further experimentation prompted by our data.

Chapter 2

Theoretical Background

The previous chapter introduced the motivation for producing a 2 to 20nm pattern in silicon. While most of the motivations are the technologies this research would enable, the ability to change the electronic properties of a material is a heavy implication. In this chapter, we intend to give an overview of the physical theory behind that motivation. For the readers who have never seen quantum mechanics before, a very simplified understanding is presented in Sections 2.1 & 2.2. Readers that have a basic familiarity with quantum mechanics can proceed to Section 2.3.

2.1 Quantum Mechanics Overview

The word quantum, latin for 'how much,' refers to the discretization of physical quantities, such as energy. Quantum mechanics dictates that every part of the universe can be broken down to a basic component. Electricity is broken down to electrons. Light is broken down to photons. All "quantum particles" [QP], including electrons and photons, act as both a particle and a wave[1]. Through the efforts of Planck, Einstein & de Broglie, it was found that every quantum particle has an associated energy according to [27]:

$$E = h\nu,$$

---

[1] Refer to Chapter 3 of reference [27] for a listing of the experiments that lead to this conclusion.

where E is energy, h is Planck's constant[2] and ν is the wavelength associated with the photon. This equation dictates that all QPs have energy levels which are allowed and others which are not. The interactions of a quantum particle with its environment is what determines which are and which are not allowed energies.

2.2 Particle in a Box

The quintessential example of how environment affects a quantum particle's energy level is that of a "particle in a box". As illustrated in Figure 2-1, the particle in a box is a 1-dimensional model of a QP confined by "walls" of potential (energy) greater than that of the particle.

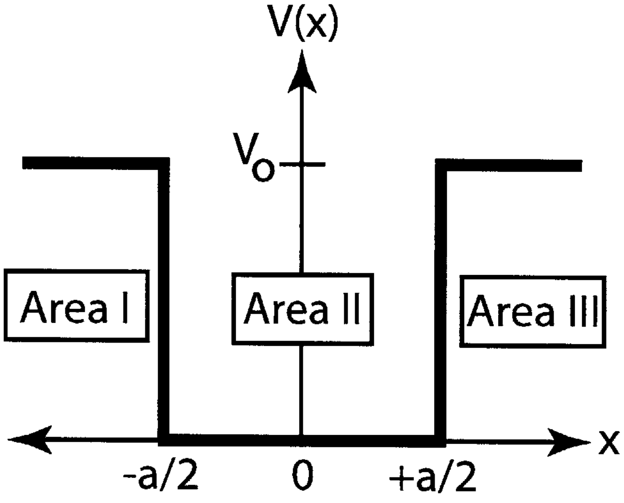

Figure 2-1: An illustration of the potential well. V_o is the height of the well and a is the width of the well.

In classical physics, the behavior of a ball in a well is governed by Newton's equations. In 1925, Erwin Schrödinger developed a analogous equation that would account for the wave properties of quantum particles [28]. In its general form, the

---

[2] $h = 6.63x10^{-34}$ J$\cdot$ s

Schrödinger equation[3] is:

$$i\hbar\frac{\partial}{\partial t}\Psi(x,t) = -\frac{\hbar^2}{2m}\frac{\partial^2}{\partial x^2}\Psi(x,t),$$

where $\hbar$ is Planck's constant divided by 2π, m is the mass of the particle and $\Psi(x,t)$ is the wavefunction of the particle. Heisenberg's uncertainty principle states that it is not possible to know the exact location of a particle without destroying all other relevant information (i.e. direction and speed) [27]. Thus a wavefunction can be thought of as a probability of where the particle is located, based on time (t) and position (x).

For the purposes of the experimental work in this thesis, we need only consider the time-independent version of the Schrödinger equation:

$$E\psi(x) = -\frac{\hbar^2}{2m}\frac{\partial^2}{\partial x^2}\psi(x), \tag{2.1}$$

where E represents the energy of the QP. $\psi(x)$ for the time-independent Schrödinger equation is a summation of sines and cosines, as derived in Appendix A.

In a quantum well with walls of infinite potential,

$$\psi(\pm\frac{a}{2}) = 0,$$

where a is the width of the quantum well.

In the case where the walls of the quantum well are finite, the wavefunction is *non-zero* at the walls of the well. Instead, there is an exponential decay in the probability of finding a particle within the wall. If two finite quantum wells are close enough, the exponentially decaying probabilities will overlap. Thus there is a finite probability that a particle could transfer from one well to another. If applied to the macroscopic world, this statement would mean that if we threw a tennis ball at a wall enough times with enough force, there is a chance the tennis ball will pass through the wall, without actually damaging the wall or the ball! This QM phenomenon is known as

---

[3] For a complete derivation of Schrödinger's equation, please refer to Chapter 4 of reference [27].

quantum tunneling.

Before we can delve into quantum tunneling further, we must first understand how a particle behaves in a lone finite well. To do this, we will break the quantum well into three parts. As depicted in Figure 2-1, we will call the left wall, well and right wall areas I, II & III, respectively. Each area has it's own corresponding wavefunction, $\psi_{area}(x)$. Since the wavefunction of the particle in the box needs to be continuous, we need to set the functions, and the derivatives of the functions, equal to each other at each boundary:

$$\psi_I(-\frac{a}{2}) = \psi_{II}(-\frac{a}{2}) \qquad \frac{\partial\psi_I(-\frac{a}{2})}{\partial x} = \frac{\partial\psi_{II}(-\frac{a}{2})}{\partial x} \tag{2.2}$$

$$\psi_{II}(+\frac{a}{2}) = \psi_{III}(+\frac{a}{2}) \qquad \frac{\partial\psi_{II}(+\frac{a}{2})}{\partial x} = \frac{\partial\psi_{III}(+\frac{a}{2})}{\partial x} \tag{2.3}$$

Solving these equations will provide a solution to the finite potential well.[4]

To understand how a particle acts in different width quantum wells, envision all the strings of a harp. Each string resonates at a set frequency. The shorter the string, the higher the frequency. The same holds true for quantum wells. As the width of the quantum well becomes smaller (meaning the confinement is higher) the allowed energy levels increase in energy.

2.3 The Kronig-Penney Model

In this thesis, we propose methods of creating patterned nano-holes in a substrate. Quantum mechanics plays a major part in how these nano-holes will modify the substrate's properties. As we decrease the spacing between these nano-holes, the chances of tunneling between wells increases. The wavefunction of the particle in the quantum well thus needs to be modified to include the presence of nearby quantum wells.

Now imagine infinite quantum wells in one direction, all spaced at the same small distance from each other. We intuitively acknowledge that a particle will behave the

---

[4] Refer to Appendix B for the complete derivation of the solution to the finite potential well.

same way in any quantum well within the infinite string of quantum wells. Instead of solving the string of infinite quantum wells as a system, it is more efficient to decipher the wavefunction in one quantum well, and then replicate this wavefunction to all the other quantum wells. This is the basis for the Kronig-Penney Model.

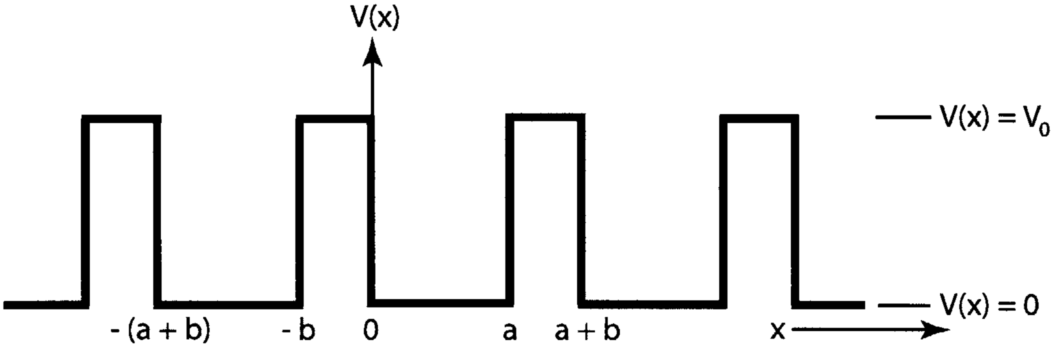

Figure 2-2: The square-well periodic potential as introduced by Kronig and Penney.

2.3.1 Derivation

To derive the solutions within the square-well periodic potential illustrated in Figure 2-2, we must first look back to the lone finite potential well. Referring to the labels in Figure 2-1, area II has the following wavefunction:

$$\psi_{well} = Ae^{iKx} + Be^{-iKx}, \tag{2.4}$$

which is a linear combination of plane waves traveling to the right and left. A and B represent variables which must be solved dependent on the particle-well interaction. K is related to energy, ϵ, according to:

$$K = \sqrt{\frac{2m\epsilon}{\hbar^2}} \tag{2.5}$$

The wavefunctions of areas I & III of the quantum well (see Figure 2-1) have a linear combination of exponentials:

$$\psi_{wall} = Ce^{Qx} + De^{-Qx}, \tag{2.6}$$

where C and D again vary on the particle-environment interaction and

$$Q = \sqrt{\frac{2m(V_0 - \epsilon)}{\hbar^2}}\,. \tag{2.7}$$

Now that we have solutions for the lone finite potential well, we need a method of extending the solutions to a periodic structure, as in Figure 2-2. We therefore look to the Bloch functions [29] which hold the form:

$$\psi_{\mathbf{k}}(\mathbf{r}) = u_{\mathbf{k}}(\mathbf{r})\ \exp(i\mathbf{k}\cdot\mathbf{r}), \tag{2.8}$$

where **k** is the wavevector and **r** is the direction of the particle in the periodic potential. Within the Bloch format, $u_{\mathbf{k}}(\mathbf{r})$ sets the potential periodicity and $\exp(i\mathbf{k}\cdot\mathbf{r})$ represents the phase of the particle wavefunction.

If we again look back to the finite potential well in Figure 2-1, we can see that if a number of these wells are stacked close together, area I from one well will be adjacent to the next well's area III. Thus we can combine Equations 2.2 & 2.3 with the finite potential wavefunctions 2.4 & 2.6 and put them into the Bloch form of Equation 2.8. Doing so at $x = 0$ we calculate [29]:

$$A + B = C + D; \tag{2.9}$$

$$iK(A + B) = Q(C - D), \tag{2.10}$$

and at $x = a$:

$$Ae^{iKa} + Be^{-iKa} = (Ce^{Qb} + De^{-Qb})e^{ik(a+b)}; \tag{2.11}$$

$$iK(Ae^{iKa} + Be^{-iKa}) = Q(Ce^{Qb} - De^{-Qb})e^{ik(a+b)}, \tag{2.12}$$

where a refers to the width of the well and b is the width of the wall, as depicted in Figure 2-2.

Equations 2.9 through 2.12 only have a solution if the determinant of the coefficients of A, B, C, D vanishes [29], or if:

$$\frac{Q^2 - K^2}{2QK} \sinh Qb \, \sin Ka + \cosh Qb \, \cos Ka = \cos ka. \tag{2.13}$$

This equation was first used by Kronig and Penney to solve for the allowed energies in the square-well periodic potential that they introduced.

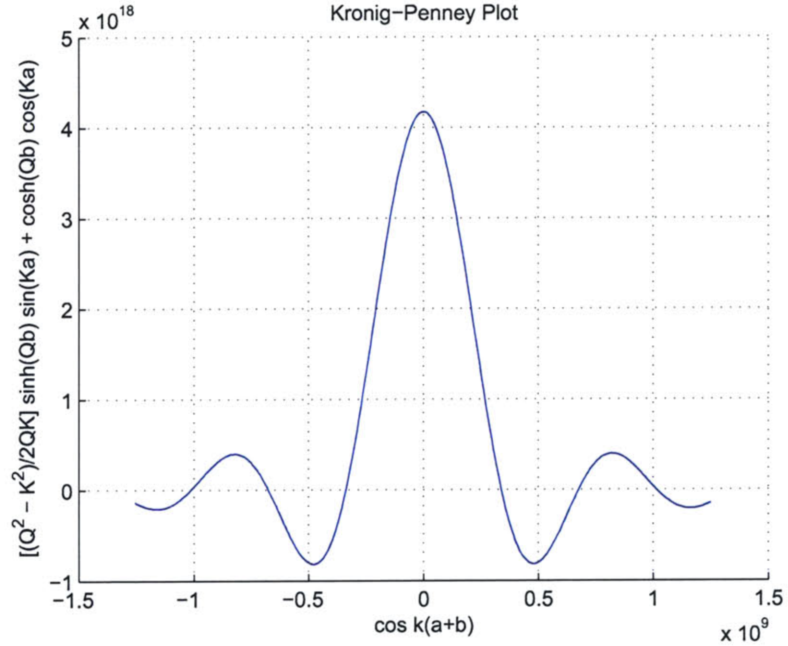

Figure 2-3: A plot of the two sides of the Kronig-Penney Relation. Values based on a 9nm wells spaced 6nm apart in intrinsic silicon.

2.4 Kronig-Penney Simulations

To determine the allowed energies in nano-porous silicon, Equation 2.13 needs to be solved. Appendix C lists the Matlab code used to achieve the allowed energies and diagrams listed in this section.

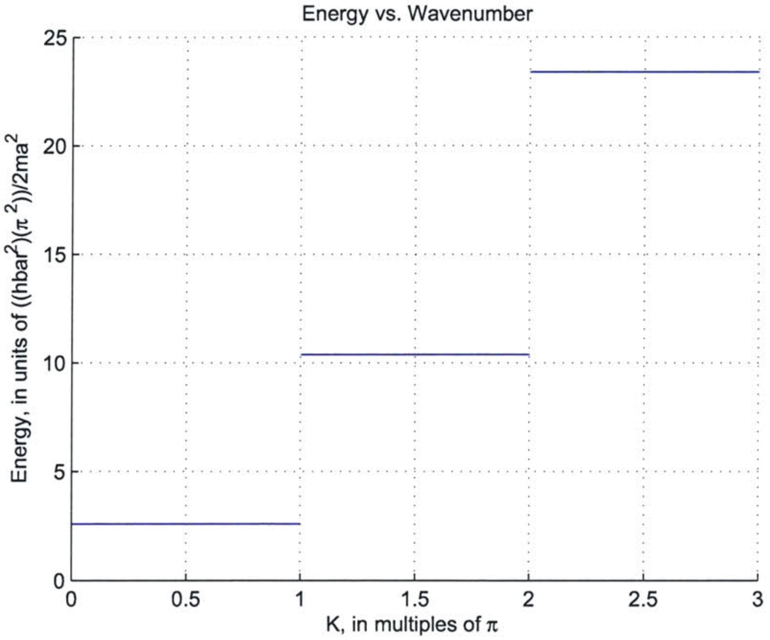

Figure 2-4: Plot of energy vs. wavenumber for the Kronig-Penney potential with 9nm wells spaced 6nm apart.

Let us first analyze how the band structure is modified based on the feature sizes we currently are attempting to achieve. Based on the approximate dimensions of feature sizes achieved in Chapter 9, we will use a well width of 9nm and a potential wall width of 6nm. The potential V_0 used is 4.7eV, the work function of intrinsic silicon - the desired patterning substrate. Using these values, the two sides of Equation 2.13 are plotted against each other in Figure 2-3 to find the discrete energy value, or eigenvalues, of the system. Once these eigenvalues are determined, they are plotted against wavenumber in Figure 2-4. The energy is plotted among the same range of wavenumbers in Figure 2-5, where the separate allowed energies become readily apparent in a band-type structure, or band diagram.

There is little dispersion present in the energy versus wavelength plot of Figure 2-4. Let us thus attempt smaller features. Figure 2-6 presents the band structure of 2nm wells with 4Å spacing in intrinsic silicon[5]. We begin to see energy dispersion for the different particle wavenumbers. How does this affect the particle behavior? Let

---

[5] All further chapter values, calculations and diagrams can be assumed to be based on intrinsic silicon, unless otherwise noted.

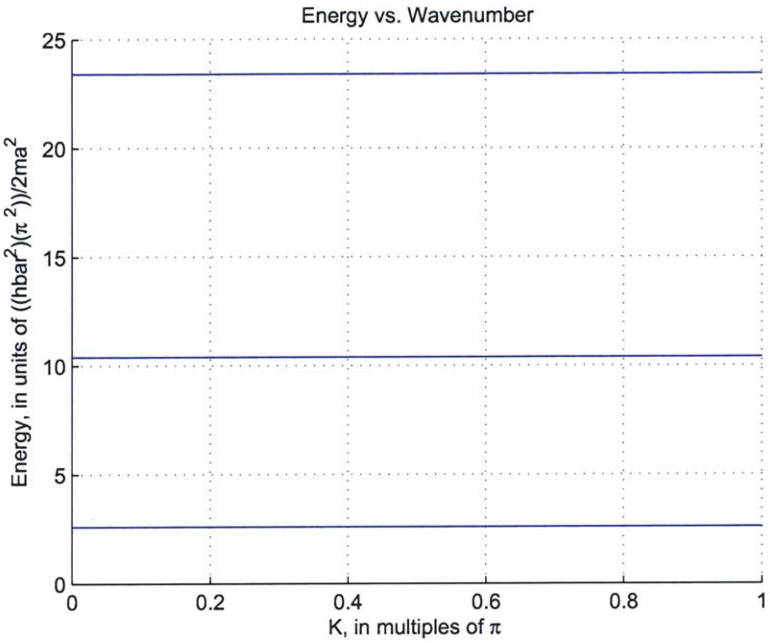

Figure 2-5: Band diagram of 9nm wells with spacing of 6nm.

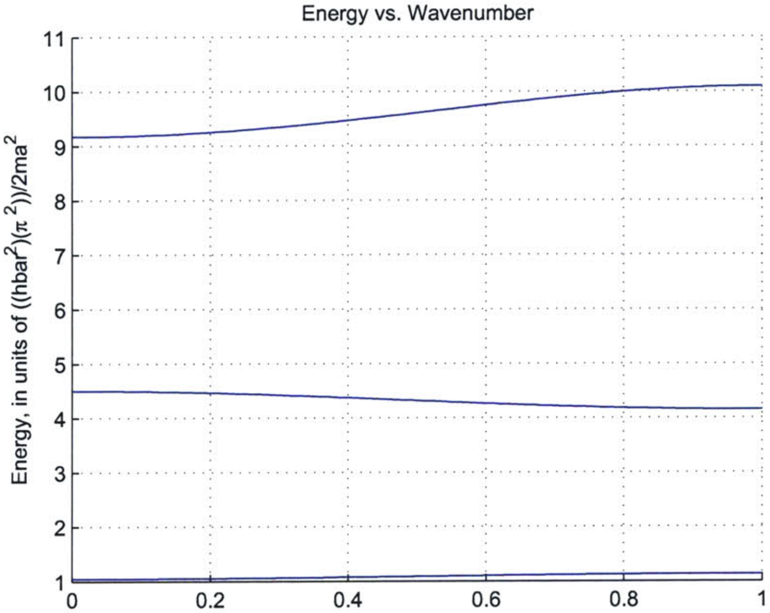

Figure 2-6: Energy vs. wavenumber for the Kronig-Penney potential with 2nm wells spaced 4Å apart.

us refer to Figure 2-7 - a plot of ψ^2, wavefunction probability, relative to the size of two adjacent wells. The height of the potential is again 4.7eV. The probabilities are all scaled up by the same factor in order to give the reader a perception of where the particle is most likely to be found for each energy level. Two wells are drawn to show the effect of the energy dispersion mentioned before. It is apparent that the higher energy levels give a greater probability of finding a particle within the well walls and of having the particle tunnel from one well to the next.

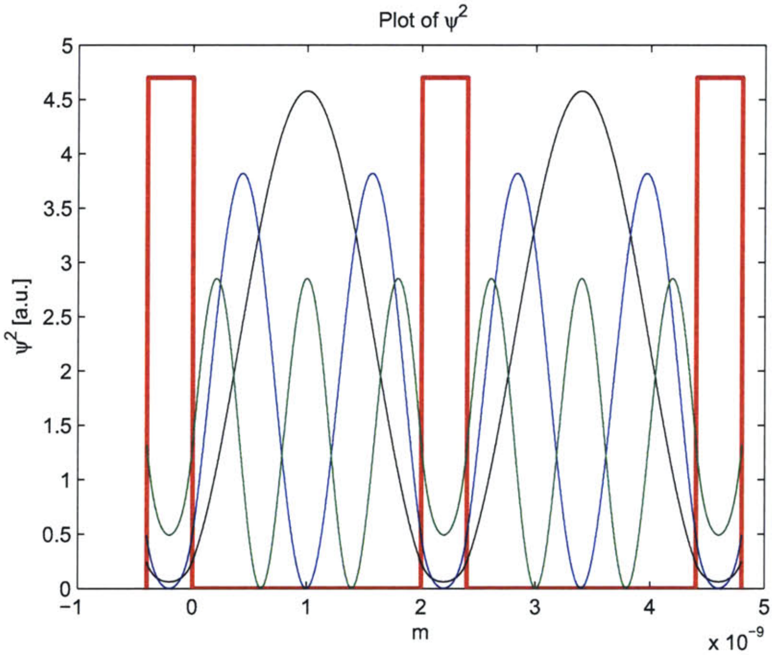

Figure 2-7: Illustration depicting scaled probabilities of particle location relative to two 2nm wells spaced 4Å apart. The first energy level is drawn in black, the second in blue & the third in green. The red potential is 4.7eV.

It seems there is a relationship between wall width and dispersion, so let us keep the well size constant and vary the wall width. Figure 2-8 shows the band diagram for 2nm wells with spacing increased to 7Å between wells. It appears that the dispersion is not as great as the dispersion seen in Figure 2-8. How does this effect tunneling probability? Figure 2-9 shows that the tunneling probability decreases compared to that displayed in Figure 2-7.

For comparison, Figure 2-10 displays the band diagram for the other extreme:

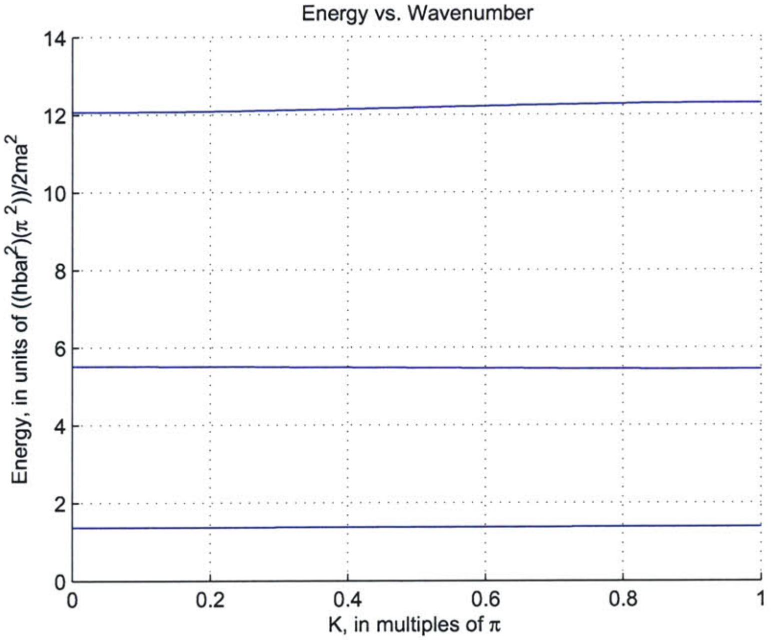

Figure 2-8: Band diagram of 2nm wells with spacing of 7Å .

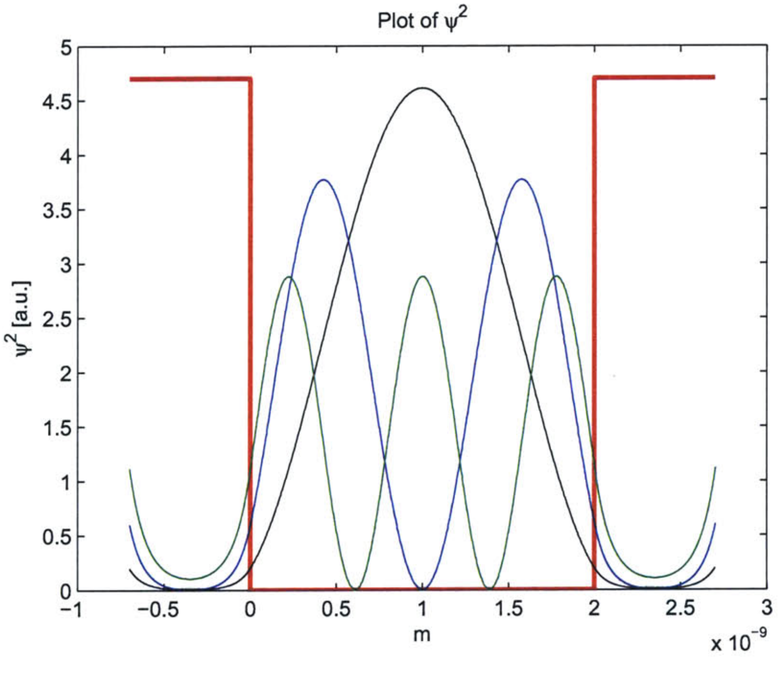

Figure 2-9: Illustration depicting scaled probabilities of particle location relative to a 2nm wells with 7Å walls. The first energy level is drawn in black, the second in blue & the third in green. The red potential is 4.7eV.

2nm wells with 1Å spacing. The particle probabilities are displayed in Figure 2-11. While 1Å would be difficult to attain, Figures 2-10 & 2-11 relay well the connection between well size, dispersion & tunneling probability.

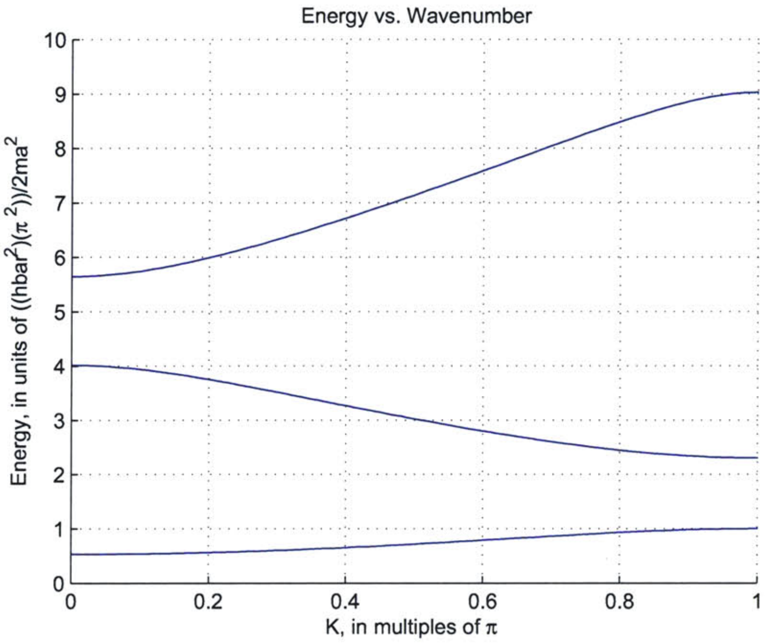

Figure 2-10: Band diagram of 2nm wells with spacing of 1Å .

2.5 Discussion

The simulations provided in the previous section show how discrete energy levels form as a result of patterning a 1-dimensional string of square nano-holes in an intrinsic silicon substrate. The 2-dimensional square lattice of cubic nano-holes problem can be separated into two orthogonal overlapping 1-dimensional problems. Thus the discrete energies calculated in Section 2.4 would be summed together to find the 2-dimensional eigenvalues.

Cubic QDs have been created [30]; thus a square lattice of cubic nano-holes in silicon is possible to fabricate. Nevertheless, the goal of this thesis is to generate hexagonally close-packed round nano-holes in silicon, a more complicated problem to solve. Both the shape of the quantum well and orientation relative to neighboring

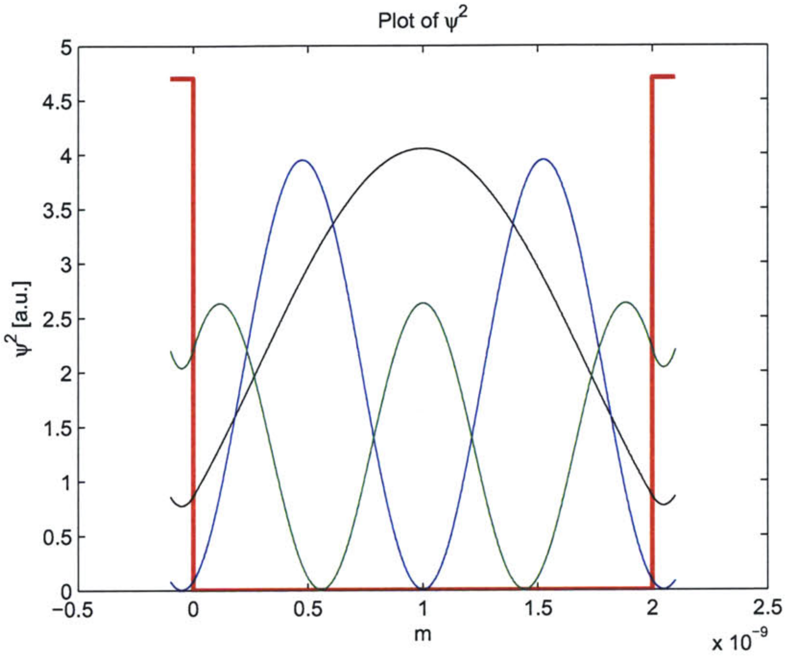

Figure 2-11: Illustration depicting scaled probabilities of particle location relative to a 2nm wells with 1Å walls. The first energy level is drawn in black, the second in blue & the third in green. The red potential is 4.7eV.

quantum wells is different from that solved in Section 2.4. Nonetheless, the problem is still a periodic potential, which the Kronig-Penney Model is based on, thus the properties illustrated throughout Section 2.4 - discretization of energy levels, dispersion & tunneling - will continue to hold.

2.6 Conclusion

In this chapter, we see the quantum effects of patterning nano-holes in an intrinsic silicon substrate. It is made clear that energy dispersion and tunneling probability both increase with decreased well spacing. We also see that discrete energy levels form at the scale of features attained in Chapter 9. The material property changes explored provide ample motivation for the thesis work explored.

Chapter 3

Analysis

The previous chapters introduced the motivation for the research detailed in this thesis. This chapter will explore the different tools used to analyze samples. Since the scale of our work is on the order of a few nanometers, very sensitive analytical methods are needed to determine whether a process has performed as desired. Thus it is important to understand the basis of operation for our analytical tools, and the strength and weakness inherent to their methods of operation.

3.1 Atomic Force Microscopy

The Atomic Force Microscope (AFM) is a tool capable of producing images with resolution down between 1 and 5nm, thus it is used extensively throughout our work. An AFM senses interatomic forces that occur between a probe tip and a substrate [31]. The AFM has two primary modes: contact and tapping (a vibrational intermittent contact mode)[1]. Since the contact mode can manipulate particles on a substrate or cause damage to the tip and sample, we will focus on the tapping mode of operation.

In tapping mode, the AFM vibrates the probe tip at the tips resonant frequency. Probe tips can be composed of any number of materials fabricated through many different processes; thus each tip will have a different resonant frequency. In this

---

[1] The term and technique classified by "TappingMode" is trademarked and patented by Veeco Instruments.

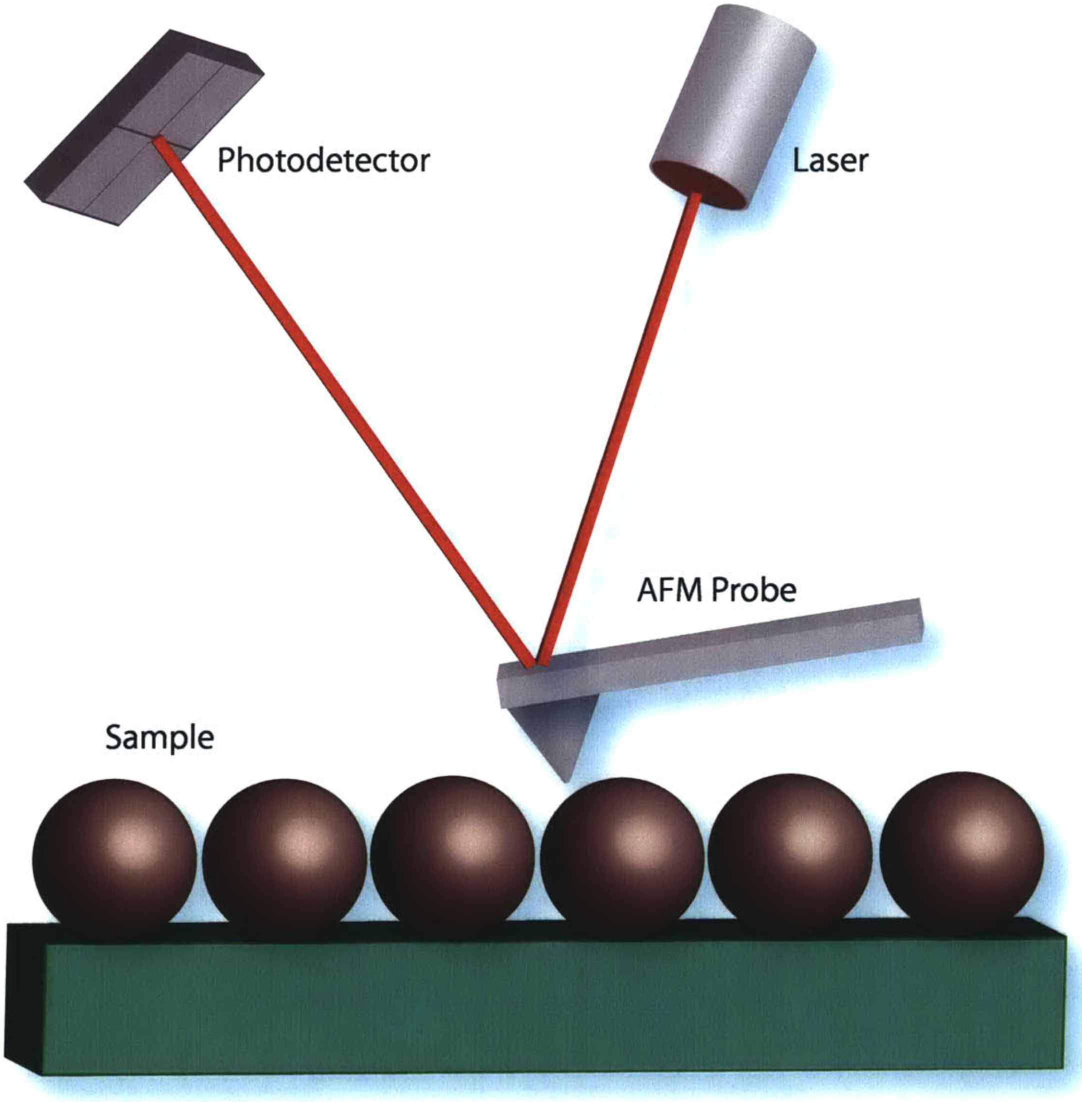

Figure 3-1: An illustration of how the Atomic Force Microscope works. A laser reflects off the AFM probe to a photodetector. When the probe deflects due to surface features, the shifted reflection registers on the photodetector.

thesis work, microfabricated silicon tips with a tip radius nominally less than 10nm were used for analysis. Once the tip's resonant frequency has been determined by the AFM, the tip is oscillated at that frequency and brought into very close proximity to the sample surface. The tip will deflect due to the repulsive forces of features on the sample surface. The larger the feature, the larger the deflection. A laser is pointed at the back side of the cantilever so that this deflection can be recorded optically. As illustrated in Figure 3-1, the reflection of the laser off the cantilever is measured by a photodetector. When the tip deflects, the laser reflection will also shift on the photodetector, again relative to the size of the sample feature. Thus the AFM is able to record the size of the feature that just passed under the vibrating tip.

The resolution of the image attained depends on the type of tip used, the flatness of the surface, the periodicity of the features on the sample surface, the speed at which the tip is passed over the surface, how many points of data are taken within a given area and how well the tip is seated within the AFM. Due to all these factors, some view taking an AFM of a sample as an art form more than a science.

3.2 Scanning Electron Microscopy

The Scanning Electron Microscope (SEM) is another very useful tool capable of attaining images with resolution down to 10nm [32]. The SEM functions by sending a stream of electrons into the surface of a sample. These incident electrons will collide with a number of atoms in the sample surface. These collisions will cause the sample atoms to emit other electrons, most notably those known as "backscattered electrons". These emitted backscattered electrons then register on a detector within the SEM. The detector in turn feeds a signal which is interpreted as different height features; the higher the feature, the more backscattered electrons detected.

While the SEM provides us with another method of viewing the surface of our sample, their are many modifications that can enhance the information obtained. The most notable for our research is a modification which allows Energy Dispersive Spectroscopy X-Ray Microanalysis.

3.2.1 Energy Dispersive Spectroscopy X-Ray Microanalysis

Energy Dispersive Spectroscopy X-Ray Microanalysis, or EDS, is a technique for observing a phenomenon that occurs when a beam of electrons is incident upon a sample surface. In addition to the backscattered electrons, x-rays are also emitted from the sample surface. These x-rays are unique to the atom that emitted them, thus a lead atom would emit different x-rays than a silicon atom. EDS merely uses a detector to observe these x-rays [32]. It then counts the prevalence of each x-ray to determine the abundance of each type of atom on the surface. As a result, EDS is very useful in distinguishing what materials are left on a surface after an chemically reactive process, such as an etch.

Chapter 4

Spin Casting

Creating a quantum dot self-assembled monolayer on a substrate is fundamental to all the later developed means of patterning. It is fitting then to first examine methods of forming or depositing a QD self-assembled monolayer. We will consider two such methods: spin casting and micro-contact printing. In this chapter, we will consider the first method - spin casting.

4.1 Introduction

As illustrated in Figure 4-1, Coe-Sullivan *et al.* [25] demonstrated that QDs will self-assemble into a hexagonally close-packed monolayer when spun out of solution. In this process known as phase separation, quantum dots are mixed with an organic solution. As this mixture is dropped onto a spinning substrate, the quantum dots and organic form two separate layers. Within a few seconds, the mixture's solvent evaporates and a hexagonally close-packed layer of quantum dots remains on top of an organic film.

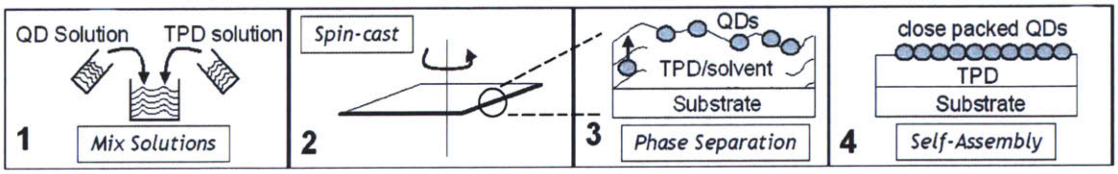

Figure 4-1: Illustration of phase separation process that occurs during spin casting.

4.2 Procedure

The spin casting procedure discussed here mimics that of Coe-Sullivan *et al.* [25]. An organic material of choice is weighed out, solvated in an appropriate solvent and stirred until all the organic material has completely dissolved. A known amount of QDs in solution is then added to the organic solution and is continually stirred. This QD-organic solution is then dropped onto a spinning substrate for a set time, at a set speed and with a set acceleration. The spinning time, speed and acceleration are adjusted to allow the solvent to fully evaporate without forcing the organic and QDs off the substrate. If all the parameters are set correctly, the result is a phase seperated bi-layer of hexagonally close-packed quantum dots on a thin film of organic.

4.3 Experimental Results

For our experiments, we used 10mg of N,N'-diphenyl-N,N'-bis(3-methylphenyl)-(1,1'-biphenyl)-4,4'-diamine (TPD) and 8mg of lead selenide (PbSe) quantum dots per 1mL of chloroform. After stirring for an hour, the solution was dropped onto a cleaned glass substrate, spinning at 3000rpm for 60s with an acceleration of 10000rpm. AFM height and phase images of the samples produced are shown in Figures 4-2, 4-3 & 4-4. The dots are easily distinguished, as is their hexagonal close-packing. In addition, grain boundaries and dislocations are clearly present in the film.

4.4 Discussion

Figures 4-2 through 4-4 are, in my humble opinion, beautiful demonstrations of the effectiveness of this procedure. Nonetheless, it is apparent that the QD monolayer is not complete and that dislocations and grain boundaries are present in the layer.

QD monolayer completeness and organic underlayer thickness can be controlled by varying the overall amount of organic and QDs in solution, as well as the ratio of the materials to each other. Through trial and error, complete QD SAMs can be produced. To minimize the number of steps involved in the trial and error process, it

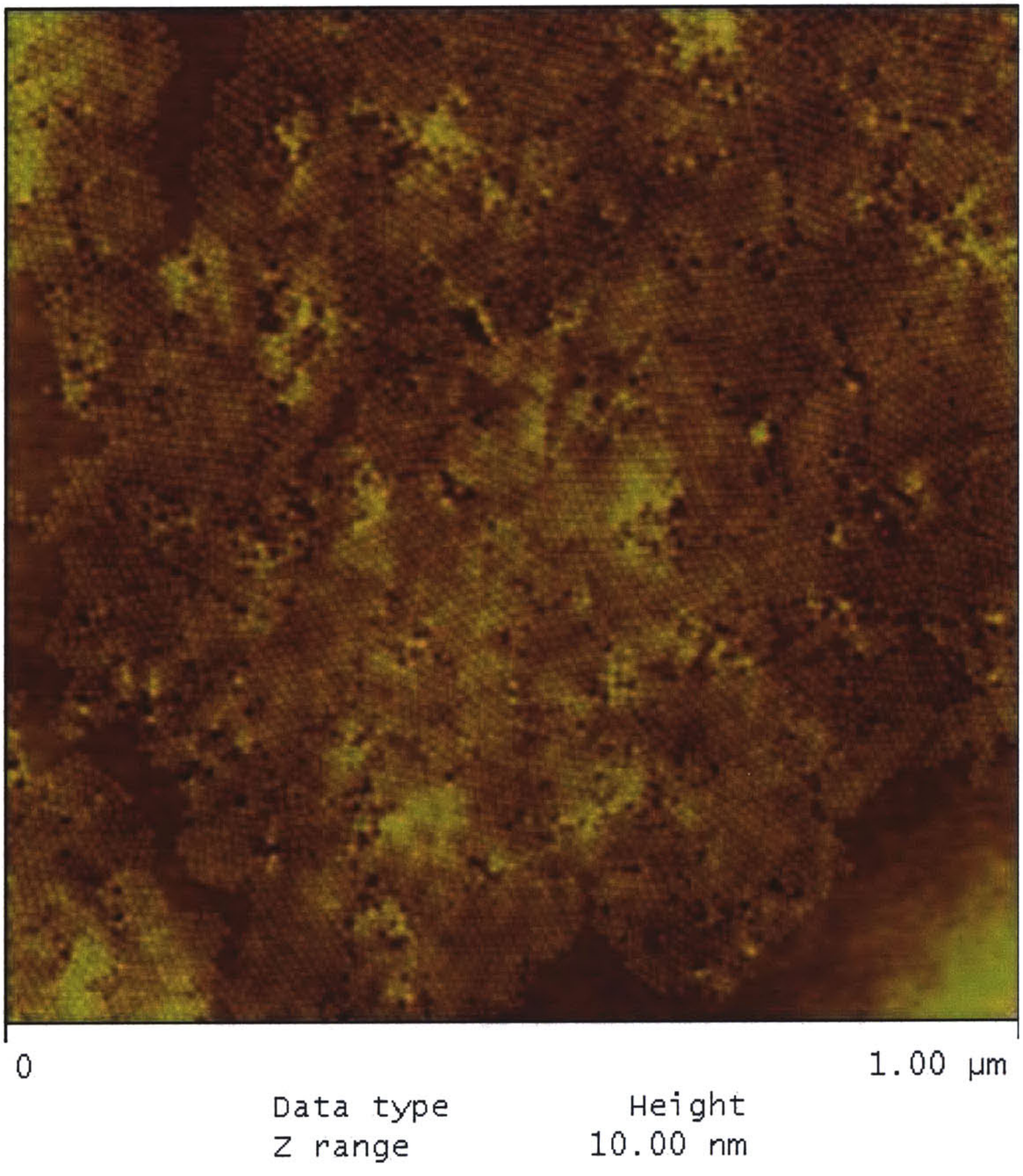

Figure 4-2: Height AFM of spun cast QD and organic solution on glass. Individual quantum dots, grain boundaries and dislocations are evident.

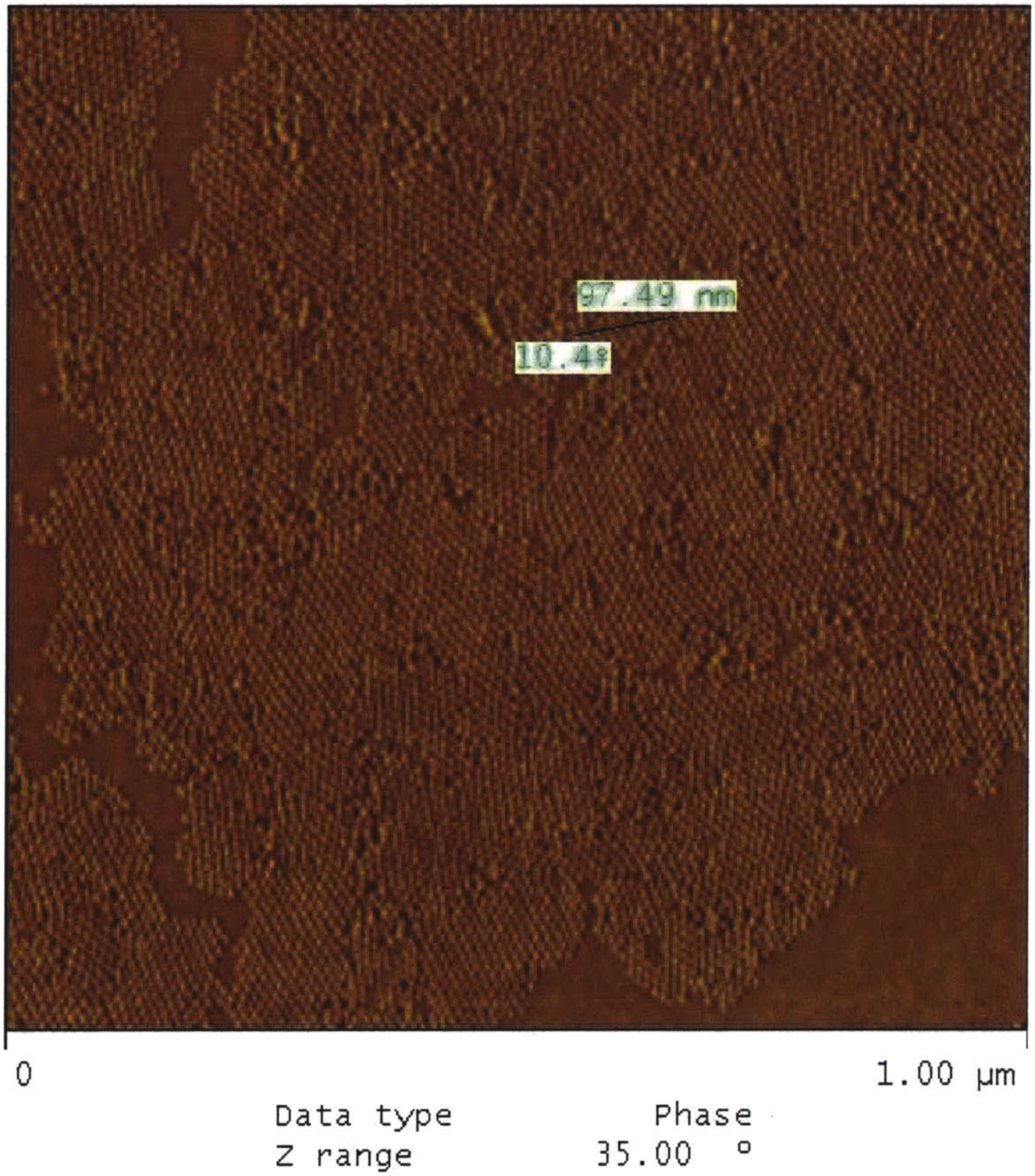

Figure 4-3: Phase AFM of spun cast QD and organic solution on glass. Approximate distance over ten PbSe dots is noted.

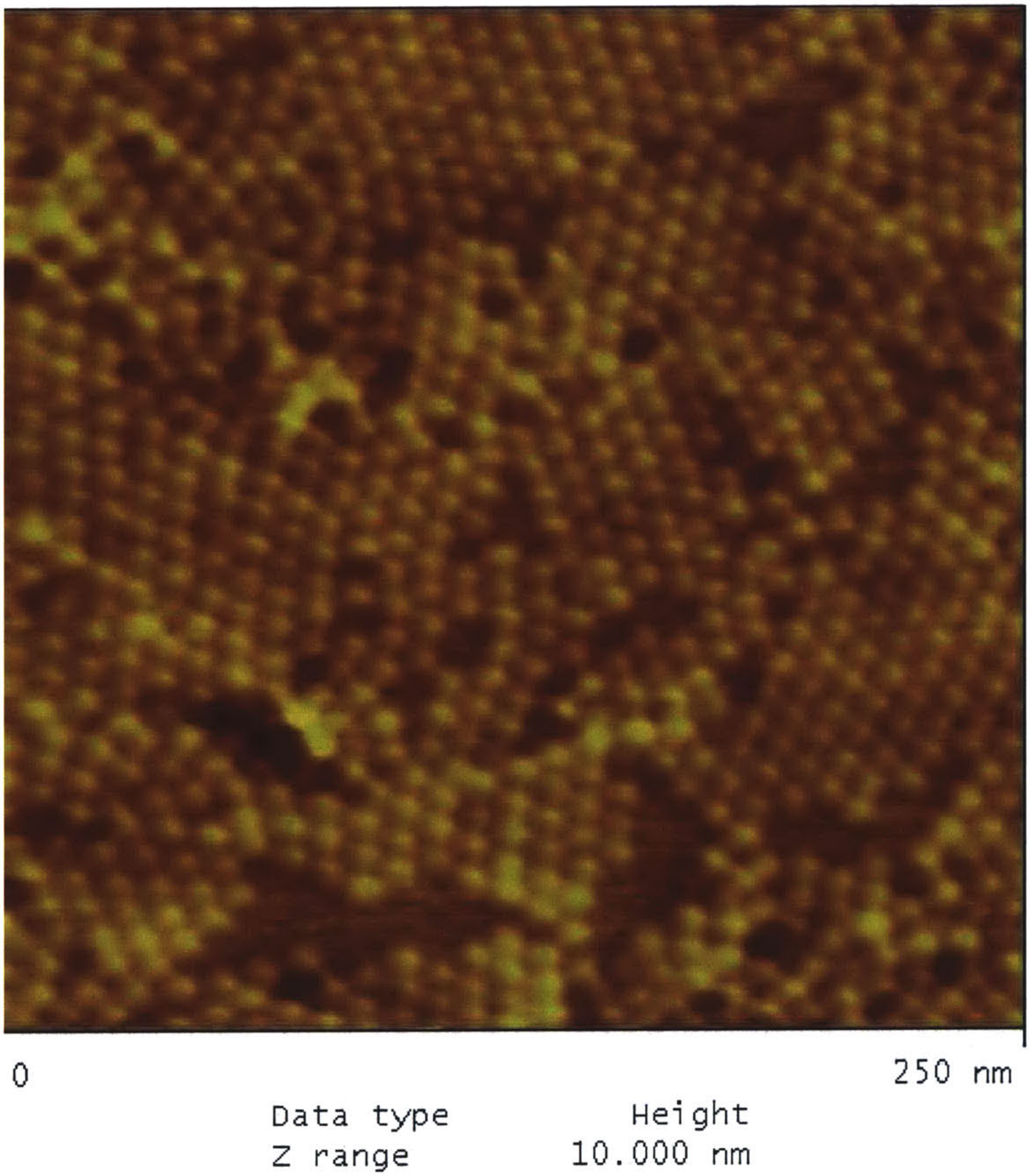

Figure 4-4: A 250nm atomic force microscopy image of the sample described in Section 4.3.

is best to first calibrate the organic and QD solutions separately. First, determine the amount of organic per volume of solvent which results in a film of desired thickness. This concentration can be extrapolated to a fairly accurate estimate of the amount of organic needed relative to the total volume of the final mixture. The same holds true for the QD solution. It is best to first calibrate a given QD solution by determining how many quantum dots are in a set volume of solvent. Unfortunately, calibration is most easily done by analyzing an AFM of a QD-organic solution which has already been spun cast on a substrate. Still, once the QD concentration of a given QD solution is determined, it can be safely assumed to be the same for all future uses.

It is important to note that if the QD concentration is saturated beyond the ratio that will produce a complete monolayer, multilayers of QDs will result. Choice of organic underlayer is also very important. The organic chosen for our experiment, TPD, was morphologically unstable and sensitive to moisture. A few days after spin-casting the film would aggregate into balls of TPD. The pronounced surface roughness would thus render the sample unfit for pattern transfer. Therefore, TPD may not be a fitting underlayer for many experiments.

4.5 Conclusion

Spin casting and phase separation were shown to be powerful tools that allow an experimenter to choose whether a complete monolayer, partial monolayer or even a multilayer of QDs is created on a sample surface. Despite the ease of the process and the ability to control many variables, the process creates a spacer layer of organics between the QDs and the substrate. This extra organic layer limits our ability to pattern, as processing steps need to be chosen so that the organic underlayer is not removed. In addition, as the space between the QDs and substrate is increased so is the chance that etch steps will not retain the pattern set by the QD monolayer. Since QDs in solution will not adhere to many spinning substrates, including silicon, it would be best to utilize another process that is able to deposit QDs directly onto any substrate.

Chapter 5

QD Micro-Contact Printing

Micro-contact printing, or “stamping”, is a technique that has been illustrated as a very simple and efficient way of depositing material from a master “stamp” to a favorable substrate [33]. Although stamping is usually associated with micro-sized feature transfer, it can be used to transfer nanometer-sized particles, including self-assembled QD monolayers [34].

There are only a few steps involved in micro-contact printing, as illustrated in Figure 5-1. Stamping obviously requires a stamp. This stamp is usually a pourable, and thus conformable, elastomer. Just as in spin casting, if QDs will not adhere to the substrate - in this case, a stamp - then another layer must be present. In spin casting, that layer is the organic which is mixed with QDs in solution. In stamping, that adhesion layer is deposited directly onto the stamp surface. Once the dots are spun onto the adhesion-layer-coated stamp, the stamp only needs to be pressed onto the desired substrate. After sufficient constant pressure is applied, the dots will transfer from the stamp to the substrate.

5.1 Experimental Results

Poly(dimethylsiloxane), or PDMS, is used as our stamping material since there already has been much work in micro-contact printing using this elastomer[33, 34]. The

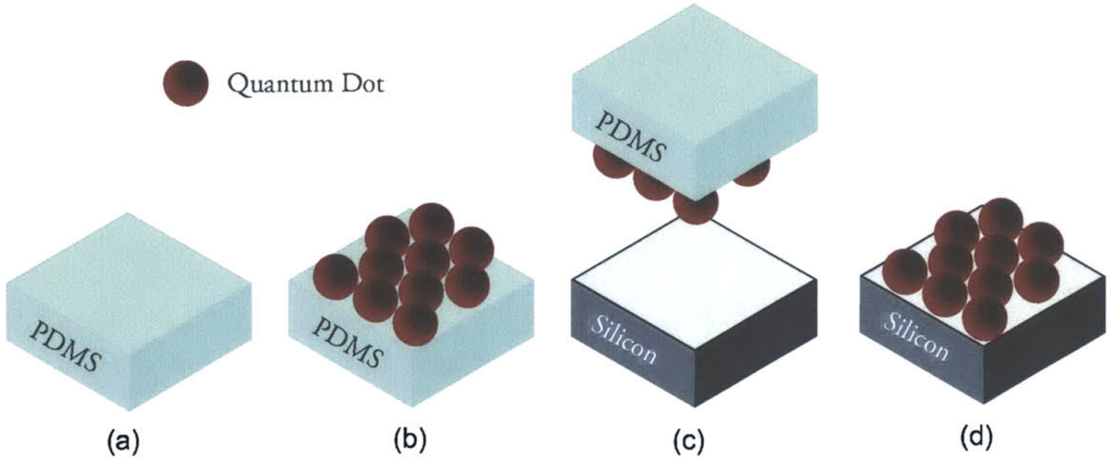

Figure 5-1: An illustration of the stamping process. (a) A PDMS Stamp. (b) QDs spun onto a Parylene-C coated PDMS stamp. (c) The QD-topped stamp is put into contact with Silicon and pressure is applied. (d) The QD layer is transferred to the Silicon surface.

PDMS[1] stamps were created by mixing a base and curing agent in a clean mixing dish. Once thoroughly stirred, the PDMS is degassed in a vacuum box and then poured into a mold. In our experimentation, 3" polyethylene petri dishes were used as molds. The liquid PDMS is then degassed to remove air trapped during transfer from the mixing dish to the mold. After about two days, the PDMS will fully cure at room temperature.[2] Once cured, the PDMS is removed from the mold and divided into cubes having the length and width of our silicon substrates.

The PDMS cubes are then coated with 0.1-2μm parylene-c (parylene) using a chemical vapor deposition process. Parylene is chosen as an adhesion layer since it is stable, readily available and the QDs will adhere to it. Afterwards, the PDMS stamps have QD solution spun cast on them. Just as in spin-casting, the concentration of the QD solution varies on the degree of monolayer or multilayer desired. Once coated, the stamps are pressed onto the clean silicon substrates for a minimum of 30 seconds. The stamp is then removed, having transferred the dot layer to the silicon.

A typical dot transfer to silicon is shown in Figures 5-2 & 5-3. Again, the individual dots, grains and dislocations are evident. One can also notice that there are

---

[1] The PDMS used was Sylgard 184.

[2] Faster curing times can be achieved with higher temperatures. Sylgard 184 documentation can be referenced online at http://www.dowcorning.com.

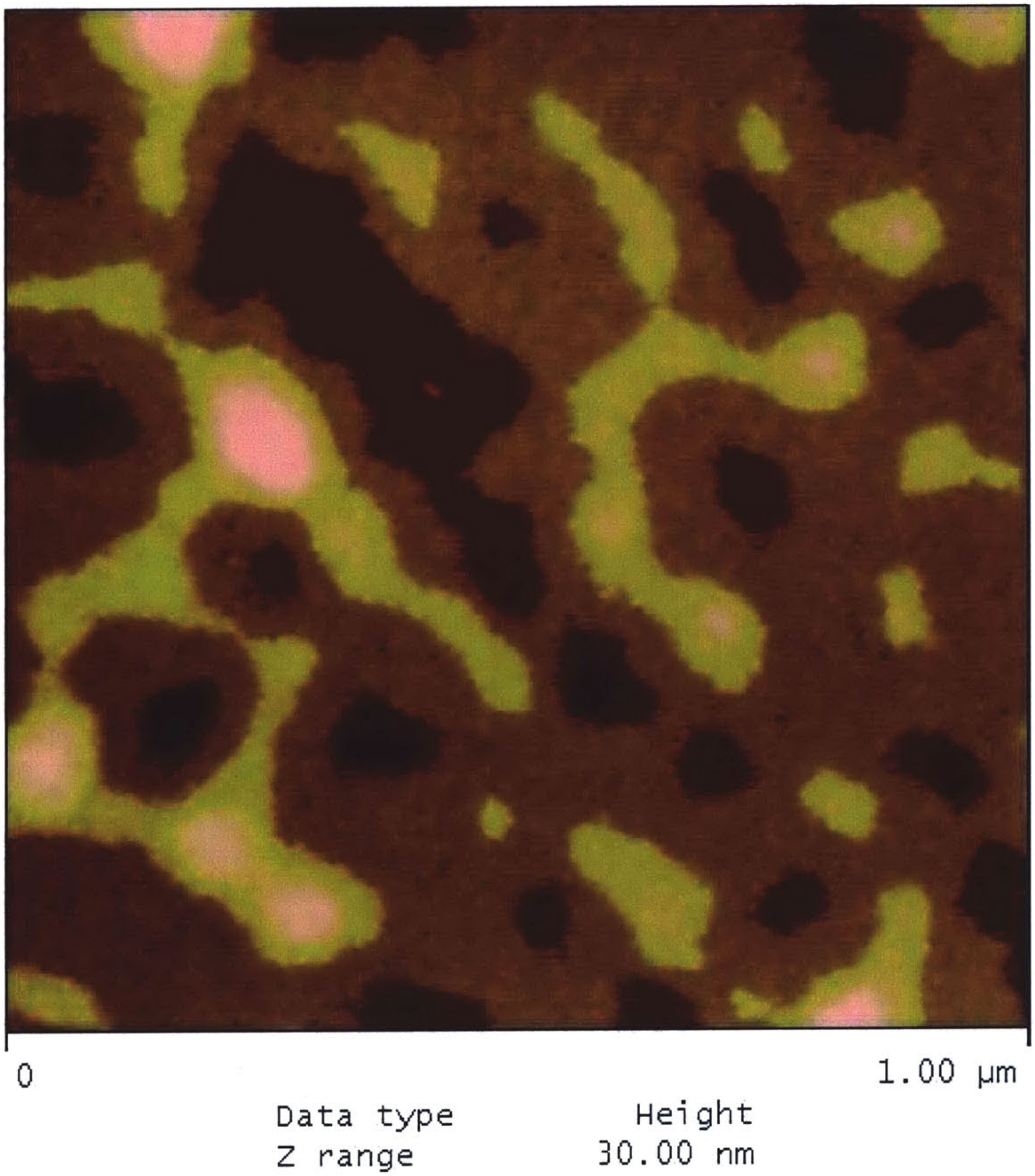

Figure 5-2: An AFM height image of a QD layer stamped onto a silicon substrate.

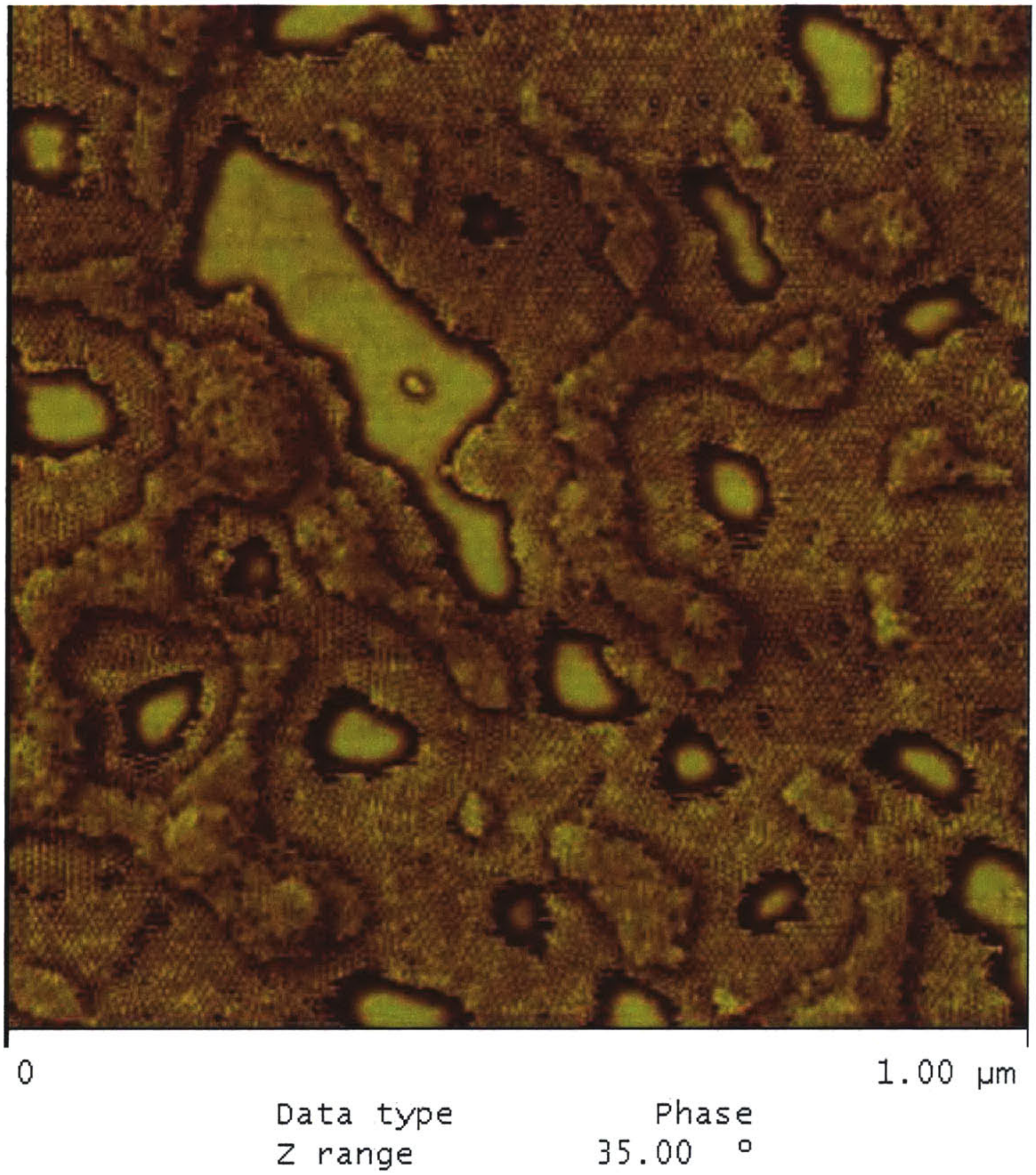

Figure 5-3: An AFM phase image of a QD layer stamped onto a silicon substrate.

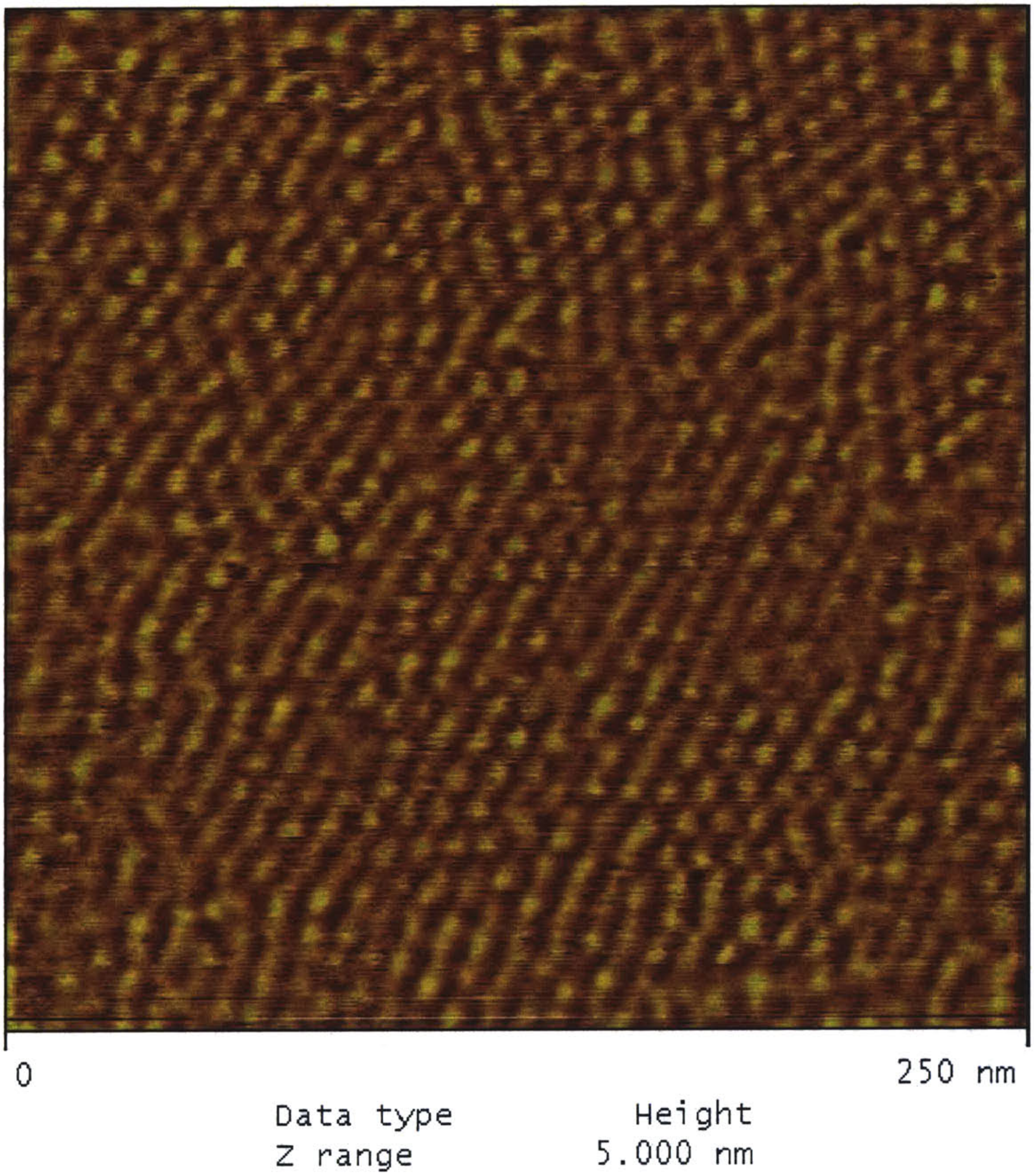

Figure 5-4: A 250nm AFM height image of a QD monolayer stamped on silicon.

more multilayers and dot "islands", or small groupings of dots, present than in the spin cast film. Nonetheless, Figure 5-4 shows that complete large grain monolayers are possible with the stamping method.

5.2 Discussion

As disccused in Chapter 4, varying QD concentration will vary the completeness of a spun monolayer. Nevertheless, multilayers are difficult to avoid using the stamping method. At the time of writing, stamping was performed manually in the Laboratory of Organic Optics and Electronics (automated systems are in development), and thus many variables are introduced into the stamping process. These include deformities in the PDMS surface and parylene layer introduced during the handling of the stamp and when the stamp is being pressed against the silicon. These deformities may create ripples in the PDMS or parylene surface which are filled by the QD solution. A roughness analysis of a blank PDMS stamp is provided in Figure 5-5. Half nanometer of roughness over nine square microns of PDMS is considered extremely flat. Parylene coating seems to reflect this same roughness, and, in some cases, it will decrease the roughness of the surface. Nonetheless, when dealing with nanometer-sized structures, this slight roughness could result in the creation of a multilayer structure.

Choice of solvent is another variable that can change results. We have performed stamps using chlorobenzene as the stamping solvent. While the stamped layers look essentially the same, chlorobenzene appears to produce longer order QD monolayers, but more multilayers. Since the vapor pressure of chlorobenzene is lower than that of chloroform, it takes a longer time to evaporate than chloroform[34]. Consequently, QDs have more time to organize into the lower energy hexagonally close-packed structure when spun out out of chlorobenzene. In addition, chlorobenzene is a higher viscosity solvent than chloroform, presumably preventing any multilayers resultant from the PDMS stamp from dispersing and filling the holes in the surrounding monolayer. Experiments with chloroform and chlorobenzene mixtures were unconclusive, which we attribute to the manual stamping process. In order to determine the ideal mixture

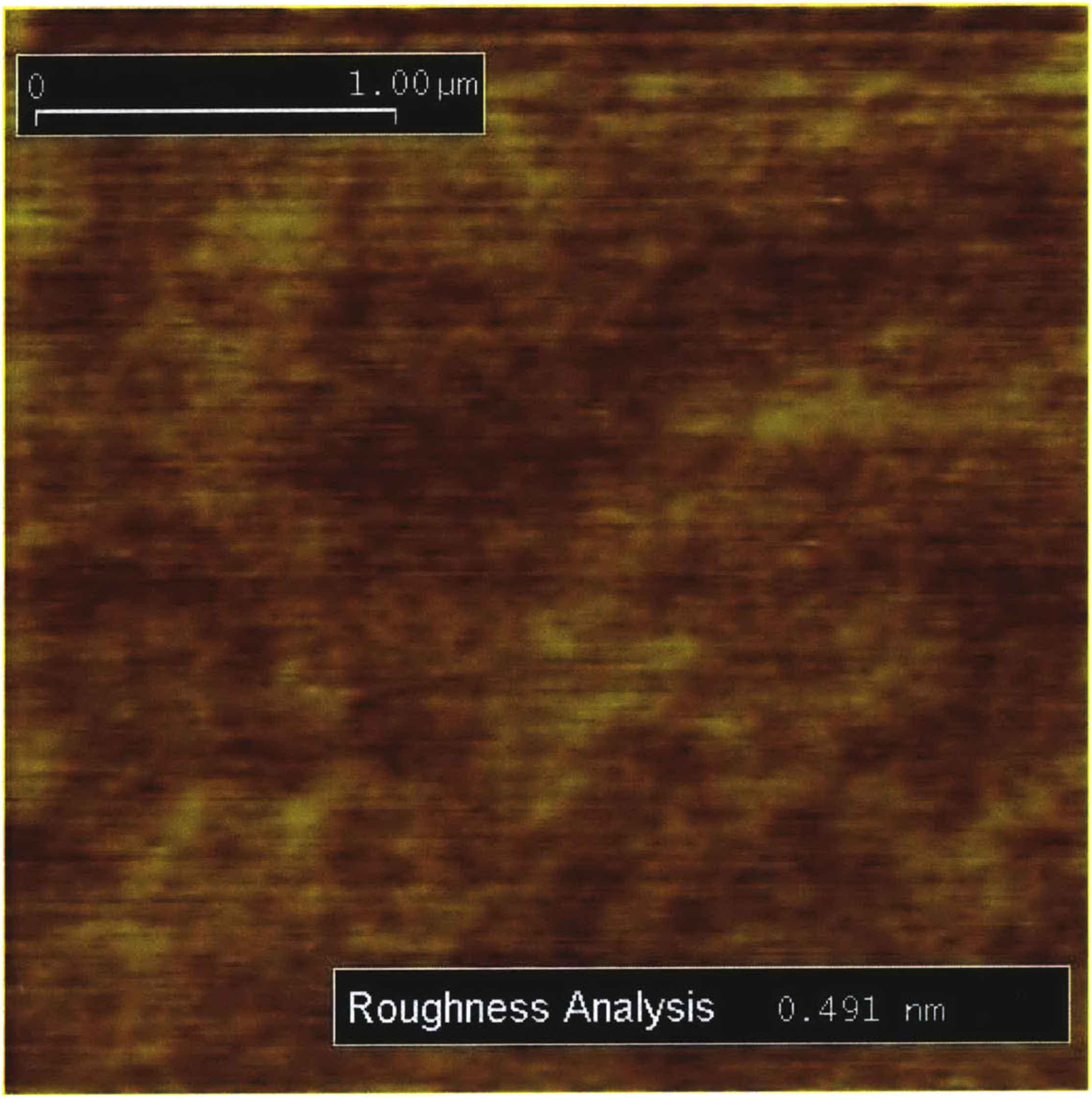

Figure 5-5: Blank PDMS AFM image with inserted roughness measurement.

of solvents, an automated system of stamping is needed.

It is also noteworthy that stamping enables the ability to place QD monolayers in arbitrary macroscopic shapes on a substrate. This already has been demonstrated [35], and can be used to further control the detail of patterning of a substrate.

5.3 Conclusion

We needed a method of depositing quantum dot monolayers directly onto substrates, and micro-contact printing delivered. Through the stamping process we were able to eliminate the QD underlayer needed in the spin cast process. In stamping, just as in spin casting, it is possible to control the monolayer completeness by varying the QD solution concentration. The disadvantages of stamping, including our current inability to control the creation of multilayers, are far outweighed by the fact that patterning steps manipulate the QD monolayer directly, without having to employ underlayer materials. Another advantage is the ability to macroscopically pattern the regions where QD monolayer are deposited. Overall, stamping is a powerful tool which we take full advantage of throughout our research.

Chapter 6

Quantum Dot Shadowmasking

The previous chapters have outlined the conceptual & theoretical motivation for our research, described QD SAM deposition & formation methods, and given an overview of the tools used to analyze our results. The following four chapters will discuss different methods of utilizing the QD SAM as a template for patterning.

6.1 Introduction

Since the QD SAM is the actual pattern to be transfered into our substrate, we first try etching the substrate exposed by the gaps between the QDs. In doing so, the QD SAM is used as a shadowmask (all that is in the *"shadow"* of the QD SAM is *masked* from etching). In order to retain the very fine feature sizes of the QD SAM, we need to use a highly directional etch, such as a reactive ion etching (RIE) process.

6.1.1 Reactive Ion Etching

The RIE process, illustrated in Figure 6-1, removes substrate material by generating chemically reactive species which form a volatile substance when in contact with the substrate [32]. RIE encompasses four primary steps: 1) an RF diode generates a glow discharge plasma[1] which produces chemically reactive species from a relatively inert

---

[1] In order for a plasma to be classified as a glow discharge, this step must occur approximately between 5 mtorr and 5 torr.

molecular gas; 2) these species diffuse to the substrate; 3) these species reacts with the substrate forming a volatile by-product; 4) the volatile gas by-product diffuses from the substrate.

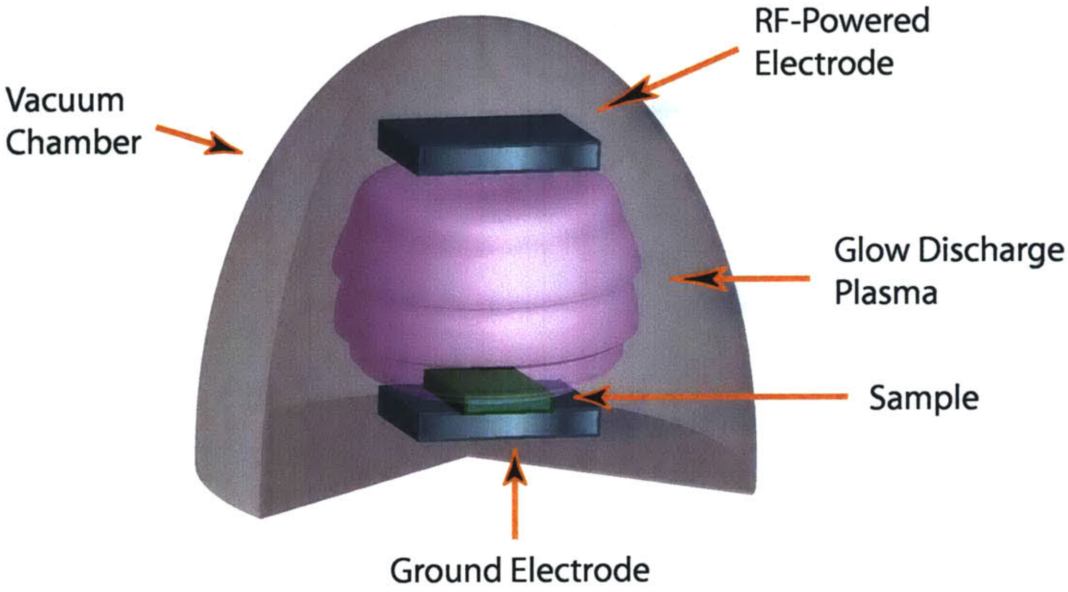

Figure 6-1: An illustration of the inside of a reactive ion etcher.

In order for a RIE to be effective, the reactive gas plasma species must *react* with the chosen substrate material. By choosing the optimal gas, the RIE can also be used to selectively etch one material out of a set of exposed materials. It is additionally important to note that lower pressures during RIE results in more vertical diffusion paths for the reactive species. In turn, as the diffusion path becomes more vertical, so does the resultant etch.

There are additional variables, which we will not discuss in detail, that can further modify RIE results. The ability to customize many aspects of an etch, including directionality, selectivity and speed, make the RIE a very useful tool which is aptly suited to our shadowmasking process.

6.2 Process

The process of using the QD SAM as a shadowmask is very simple. First, deposit a QD SAM onto a silicon substrate. Next, the substrate is placed into the reaction ion etcher. As prefaced in Section 6.1, we aim to have the reactive species pass between through gaps of the QD SAM and pattern the substrate. Since the reactive species of CF_4 etches silicon, our substrate, we use it as our inert gas.

Once the sample is loaded into the RIE, the pressure is pumped down to the minimum level that the chamber can support. This is done in order to keep the etch highly directional, thus preserving the ultra-small features of the quantum dot. Next, we strike plasma at the lowest power possible. The lower the power, the slower the etch. Even though the QDs are not the target of the CF_4 gas, they are very small and thus can only remain a short time before being etched away by a bombardment of any reactive species. For that same reason, power is supplied to the plasma for only a few seconds.

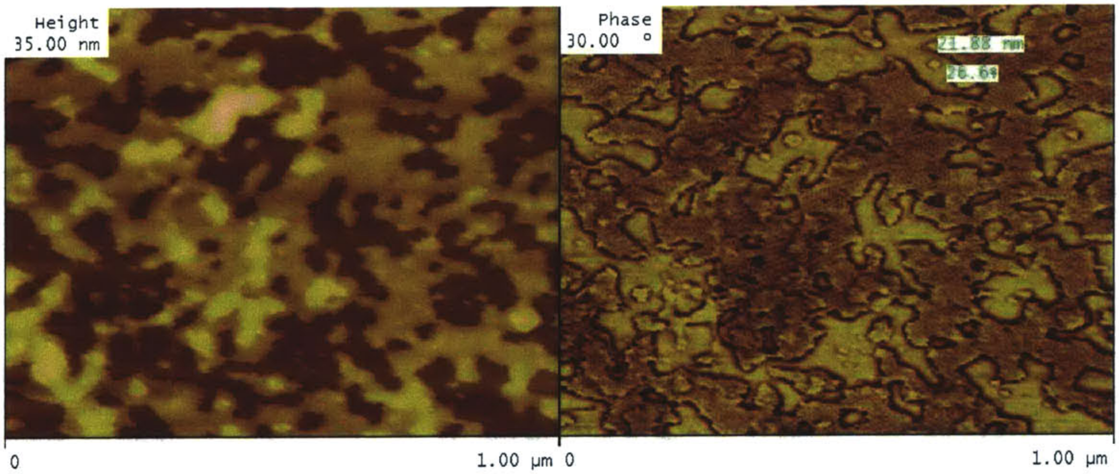

Figure 6-2: An AFM image of a QD SAM on silicon, prior to CF_4 RIE. "21.88 nm" denotes the approximate distance over *three* quantum dots.

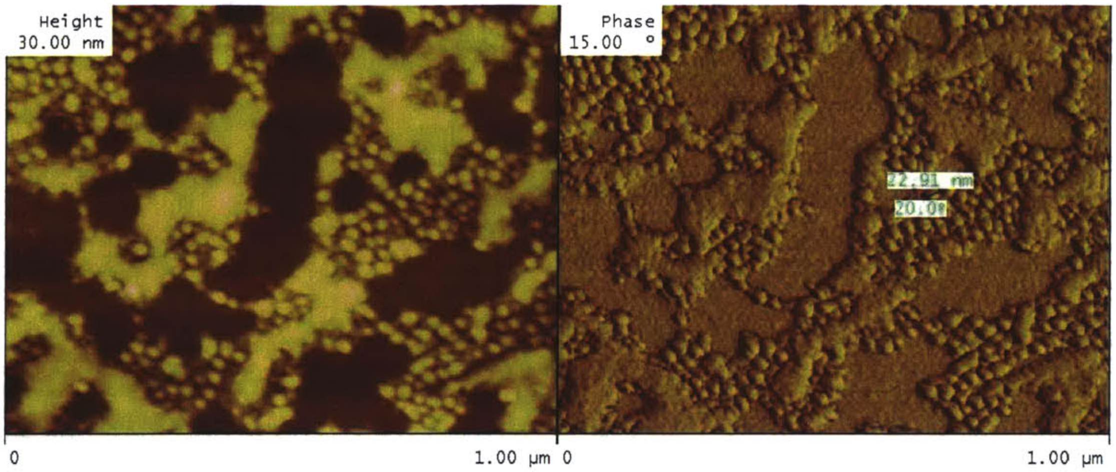

Figure 6-3: An AFM image of the QD SAM after the CF_4 RIE process. "22.91 nm" denotes the approximate distance along *one* conglomerate.

6.3 Experimental Results and Discussion

PbSe was first stamped onto silicon substrates using the procedure described in Chapter 5. A CF_4 RIE was then performed on these samples. Pressures ranging from 6 to 8mtorr, incident plasma powers from 45 to 200W and intervals between 2 seconds and 20 seconds were used. Most of the RIE experimentation was done around 60W and 7mtorr, the minimum plasma-striking power and pressure that could be reliably maintained in our RIE chamber. While Figure 6-3 is a result of a 20 second etch, all the intervals had nearly the same result: large "globules" arranged in islands similar to the outlines of the original QD SAM.

Figure 6-3 may suggest that the organic caps surrounding the QDs cross-linked when introduced to a reactive species. In order to test this hypothesis, an RIE was performed using O_2 gas and the same pressures, powers and time intervals listed for the CF_4 etch. The reactive species of O_2 is used to remove organics. Thus if the images after a O_2 etch match those of a CF_4 etch, then we can conclude that the CF_4 is actually removing, not cross-linking, the organics. The results of a 10 second O_2 etch are shown in Figure 6-5.

The O_2 result appears to be a more extreme version of the CF_4 etch. We can thus conclude that the CF_4 etch is removing the organic caps around the PbSe quantum

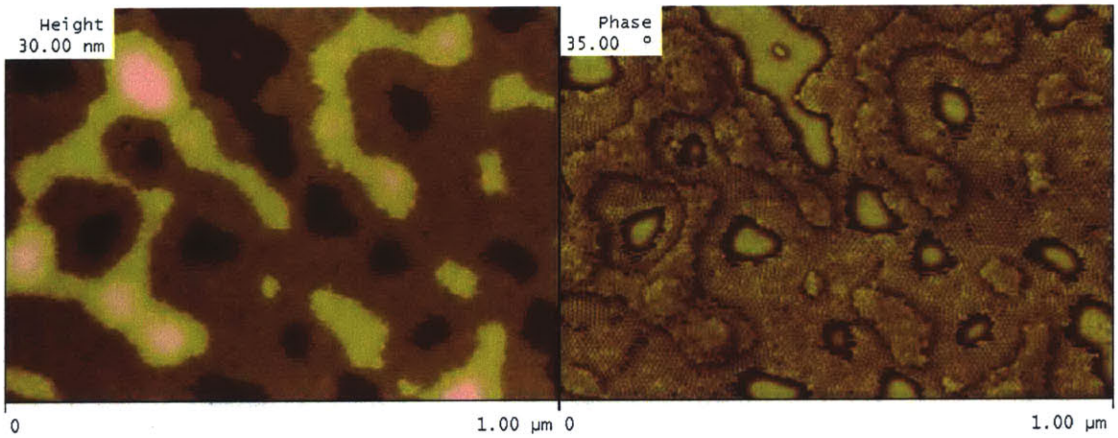

Figure 6-4: An AFM image of a stamped QD SAM before an O_2 etch.

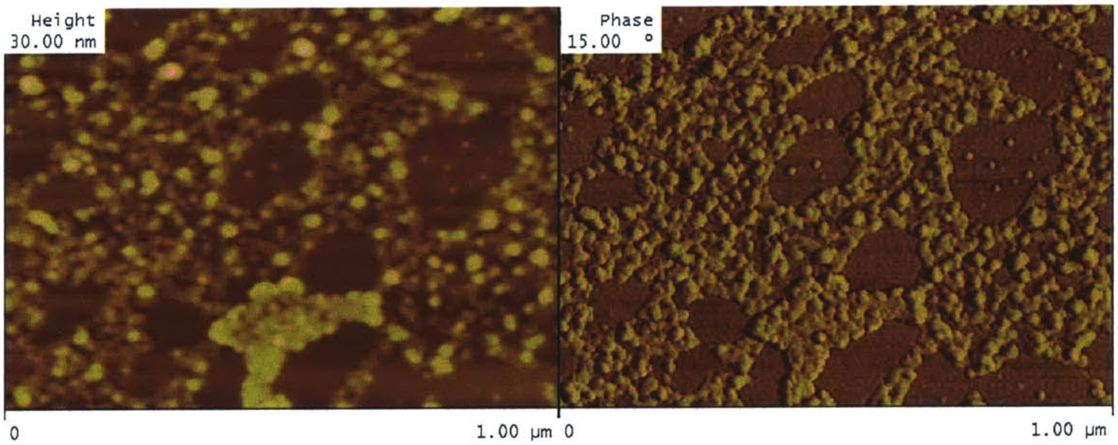

Figure 6-5: An AFM image of a QD SAM after a 10 second O_2 etch.

dots (albeit more slowly than the O_2 etch). Once the caps are gone, the QD cores sinter together, forming the conglomerates shown in Figure 6-3.

6.4 Conclusion

QD shadowmasking is the easiest and most obvious patterning technique to attempt, which is why it was tried first. While the principle is straightforward, the result is not. Theoretically, the reactive species produced during the RIE process should pass between the QDs, through the organic caps and into the silicon. In reality, the gas used to etch silicon, CF_4, quickly etches away the organic caps and the dots sinter before any patterning takes place.[2] If a reactive species is found that selectively etches silicon over organics, than this process would be very effective. Until that time, other processes need to be explored.

---

[2] While the organic blocks the CF_4 reactive species from passing through the QD SAM gaps, the outlines of the QD islands are transferred into the silicon. The slowest etch rate achieved using the listed parameters was 1Å/s, which would allow for a very controllable etch.

Chapter 7

QD Lift-Off

In the previous chapter, we attempted the most straightforward method of patterning - using the QD SAM as an etch mask. Although a simple and efficient process, RIE does not have the selectivity needed to solely etch the silicon substrate without disturbing the QD SAM. In this chapter, we look to a classic lithography trick known as liftoff to provide a possible means of patterning.

7.1 Introduction

Liftoff's concept is to deposit a material on top of a patterned "sacrificial layer", then remove (or sacrifice) that layer. When the sacrificial layer is removed, so is the material deposited on top of it. Deposited material will only remain in the areas where the sacrifical layer was not present. Thus the sacrificial layer sets the pattern for the deposited material.

7.1.1 Material Evaporation onto a Substrate

Liftoff necessitates that a thin film of a material, or a stack of materials, be deposited on a sample. Material is commonly deposited onto substrates through evaporative processes. The following sections will discuss the two most developed means of evaporation: thermal and electron beam.

Thermal Evaporation

Thermal evaporation, also known as evaporation using resistance-heated sources, is the simplest method of depositing materials [32]. A low-vapor-pressure-metal crucible is used to hold the material to be evaporated. The crucible also functions as a wire, as large amounts of current are passed through it. The resistance of the crucible to the current produces heat, which vaporizes the material in the crucible. Since this process is performed under high vacuum, the evaporated material diffuses evenly in all directions at a rate dependent on the amount of current passed through the crucible and the evaporation point of the material in the crucible.

Electron Beam Evaporation

Electron beam, or e-beam, evaporation accelerates a stream of electrons toward the material to be evaporated. Upon impact, the kinetic energy of the electrons are converted into thermal energy. This thermal energy, in turn, evaporates the material. To avoid creating a hole in the middle of the evaporating material, the stream of electrons is scanned throughout the material surface using electromagnetic deflection [32]. E-beam evaporation is also performed under high vacuum, so the mean free path of the evaporated material is longer than the distance between the material source and the sample. The e-beam evaporation rate is determined by the evaporation point for the material being evaporated and the voltage used to accelerate the electrons.

7.1.2 Wet Etching

Now that we know how to deposit material, we need to learn how to remove it. In Section 6.1.1, reactive ion etching was discussed. While RIE is directional and can be selective, some processes require a faster method of removing material throughout the sample. "Wet" chemical etching is one of the first methods of image transfer, as noted in the Introduction. Nonetheless, wet etching is still widely used, especially by the microelectronics community, because it is a relatively low cost, consistent and high throughput means of selectively removing materials [32]. It is known as *wet* etching since samples are immersed in a liquid reactant. The liquid reactant combines with molecules from the sample surface forming a reaction product. This diffusion of this product into the liquid effectively removes the material from the sample surface.

In liftoff, as mentioned in Section 7.1, a material is deposited on a sacrificial layer. That sacrificial layer then needs to be removed to leave the deposited material only in the desired area. Since liquid chemical etchants can reach any exposed material, including a sacrificial layer, wet etching is an ideal process for liftoff procedures.

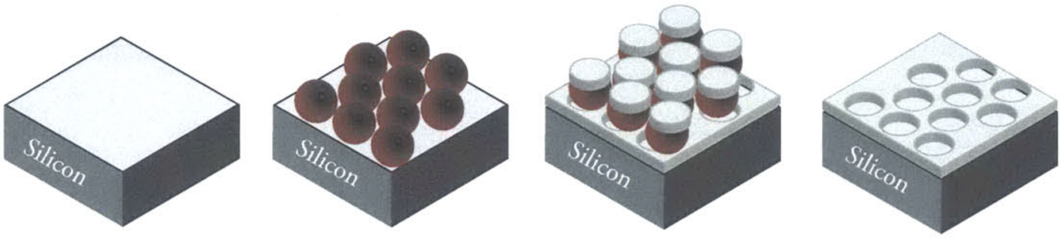

Figure 7-1: An illustration of the QD lift-off concept. A QD SAM is deposited on a silicon substrate. A metal is evaporated onto the sample, then the QD SAM is removed with an etch step. This "lift-off" step leaves metal in only the desired locations on the sample.

7.2 Process

As in Chapter 6, the QD SAM holds the pattern that we want to pass into silicon, so the QD SAM acts as our sacrificial layer. First, the QD SAM is stamped onto our silicon substrate. Next, chromium (Cr) is thermally evaporated onto the QD SAM. While many metals can be used, we choose chrome since it adheres well to silicon, can diffuse through organics (such as oleic acid caps) [36] and an etchant exists that will etch away the PbSe dots without removing chrome. This etchant is Nano-Strip[1], a stabilized mixture of sulphuric acid and hydrogen peroxide[2]. The last step is to sonicate the sample in Nano-Strip for a set time, theoretically removing the QD SAM sacrificial layer and leaving a layer of chrome on silicon with hexagonally-close-packed

---

[1] Trademarked by Cyantek Corporation.

[2] This mixture is also known as a Piranha solution.

holes approximately the size of the QDs used.

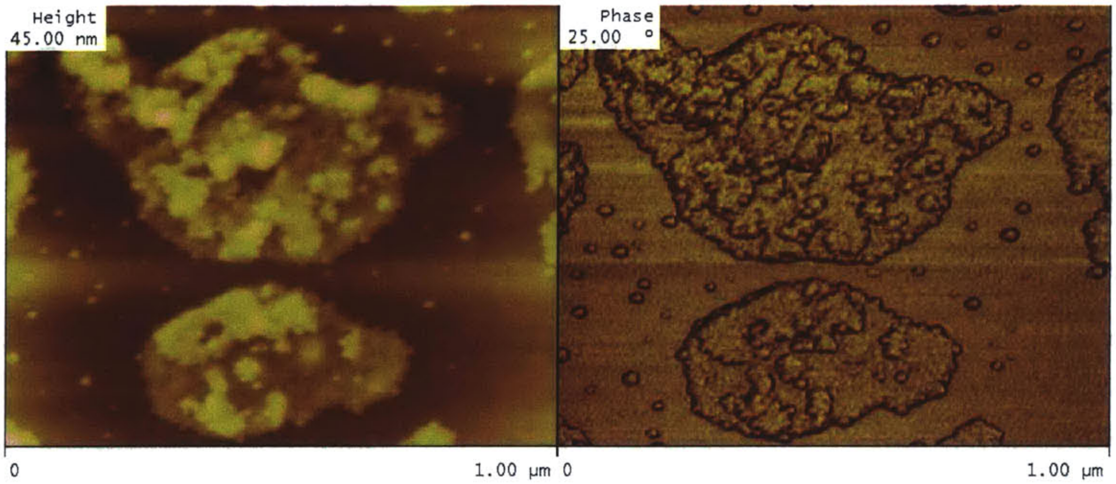

Figure 7-2: 15nm of chrome thermally evaporated onto a PbSe QD SAM on silicon as imaged in an AFM.

7.3 Experimental Results

QDs were stamped onto silicon and a SAM resulted, just as the one shown on pages 49 & 50. Figure 7-2 shows the result of a deposition of 15nm of chromium on the sample. As described in the procedure, the sample was then sonicated in Nano-Strip for 5 minutes. The result is shown in Figures 7-3 & 7-4.

It appears that the QD SAM did not function as the intended sacrificial layer. Figure 7-5 illustrates how Nano-Strip interacts with PbSe when chrome is not present. Despite the particulates remaining from the etch, it is evident that a stabilized Piranha does remove PbSe dots. What then is modified when chrome is deposited?

There are two possible theories to explain our observations. In support of the first, consider that the distances between the QDs in a QD SAM are on the order of 1.5nm. At this infintesimal distance, chrome may likely bridge the gap between dots. In addition, if the chrome fully coats the edges of the QD SAM, then no piranha solution can etch away the PbSe quantum dots. Another theory is that when the hot chrome lands on the QD SAM, the heat ablates the organic and the PbSe dots minimize surface energy by sintering with the chrome. Regardless of the reason why,

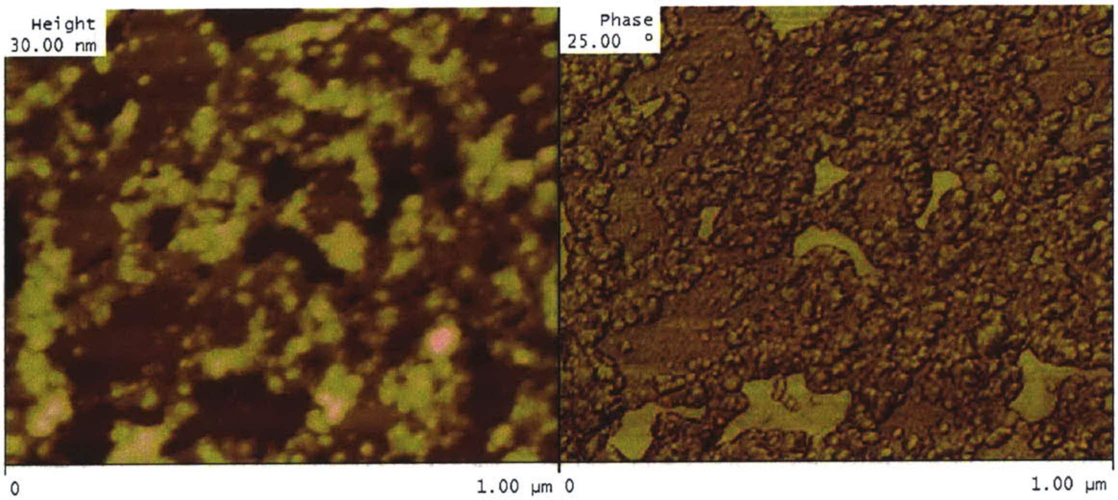

Figure 7-3: An atomic force micrograph of Chrome coated PbSe QD SAM on silicon after a 5 minute sonication in stabilized piranha.

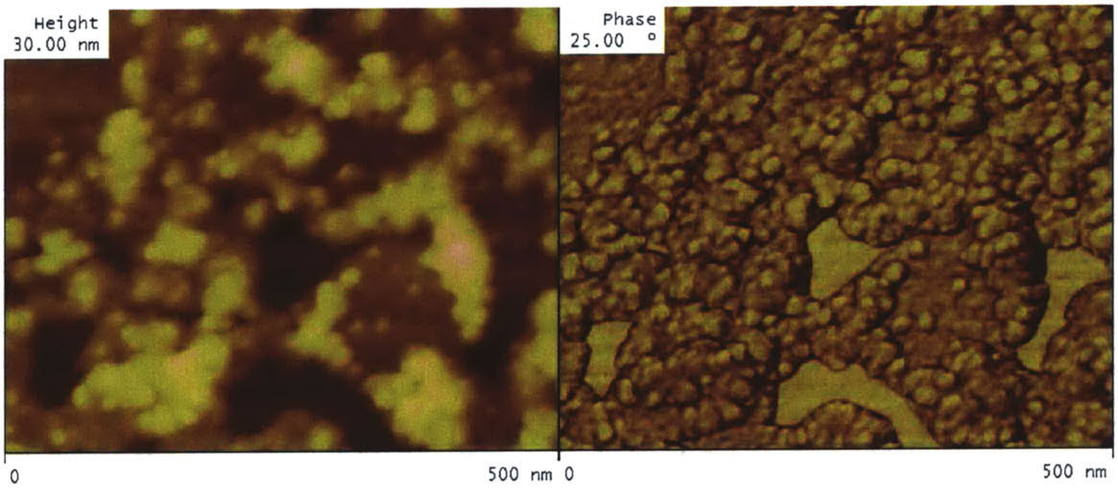

Figure 7-4: An AFM image of a Cr-coated PbSe QD SAM on silicon after a 5 minute sonication in stabilized piranha. The height scale is 500nm.

the process outlined is not effective in depositing a metal on silicon in a pattern dictated by the QD SAM.

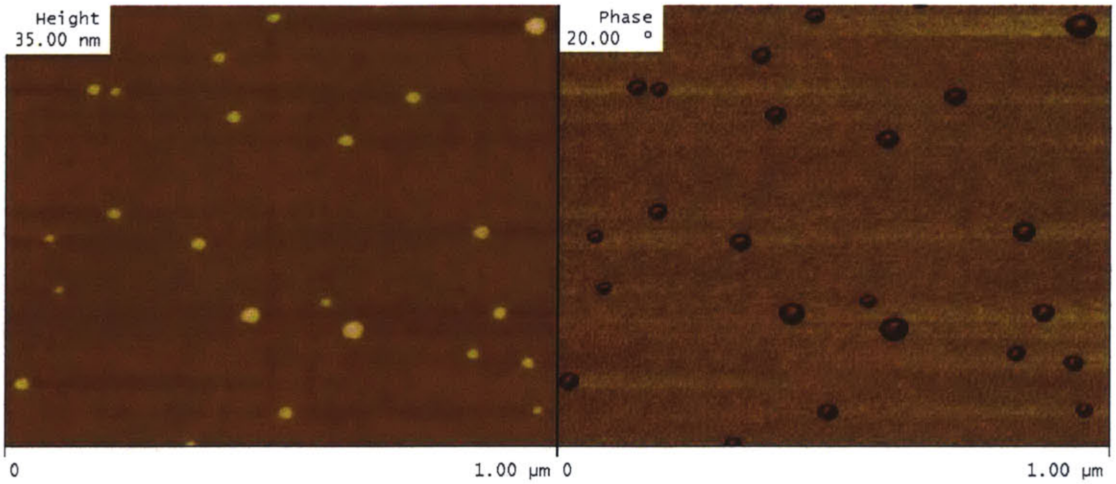

Figure 7-5: An atomic force micrograph of the surface of a PbSe QD SAM on silicon sample after a 5 minute sonication in stabilized Piranha.

7.4 Discussion

Since the above process did not have the desired results, it would be logical to also try other metals and etchants. In fact, various other metals and etchants were considered and experimented with before concluding on the above process. The first choice to consider is what metal to deposit. A metal which preferentially adheres to silicon is needed, since only a few nanometers of material are deposited. We also need a metal that can be deposited through a standard fabrication technique, such as thermal or e-beam evaporation. Lastly, we need a metal which does not react with the etchant used to remove the PbSe QD SAM. That brings us to the second point of consideration: etchant. For reasons not completely understood, PbSe QD SAMs are *unbelievably* difficult to remove once stamped onto silicon. Methods of removal attempted include directional plasma etching, decomposition through extreme heat[3], and sonication in

---

[3] Temperatures up to 400°C were used.

acetone[4], chloroform[5] and aqua regia[6].

Only two methods of stamped PbSe QD SAM removal have been discovered by the author. The first is a piranha etch.[7] The second method of removal is through mechanical means. If the silicon substrate is used itself as a stamp, the PbSe can be transferred to another substrate. This concept will be discussed further in Chapter 9. Nonetheless, of these two methods, only one can be used for liftoff: a stabilized piranha etch. Therefore, the procedure listed in Section 7.2 is the only currently feasible method of accomplishing liftoff using a QD SAM sacrificial layer.

7.5 Conclusion

In the microelectronics world, liftoff is a very effective means of patterning. Unfortunately, the liftoff process becomes rather complicated in the size scale of a few nanometers. Just as in the case of QD shadowmasking, the materials and processes do not currently exist which allow QD lift-off to occur. Nonetheless, the basis for such a procedure is detailed in the chapter above.

---

[4] A strong solvent.

[5] PbSe QDs are solvated in chloroform.

[6] A strong etchant composed of hydrochloric and nitric acids.

[7] A stabilized piranha etchant which would not attack chrome was used in experimentation. Nonetheless, a regular piranha will still etch away the PbSe QDs.

Chapter 8

Selective QD Ablation

In the previous two chapters, two methods of patterning were attempted. Both were unsuccessful due to the same problem: etching selectivity. Therefore, a method of selectively removing quantum dot material needs to be pursued. In this chapter, the idea of selectively ablating different quantum dots is described and results are given.

8.1 Introduction

There has been extensive research on using lasers to clean substrates, including glass [37] and silicon [38]. If we treat quantum dots as particles to be cleaned off a substrate, laser ablation may provide the selectivity needed for patterning. Yet, rather than use laser ablation to "etch" away QDs for another process (i.e. liftoff), laser ablation can be used to selectively create a sub-pattern within the QD SAM. Ablating one QD at a time would be too difficult and time consuming to achieve, so how do we accomplish this? A sub-pattern may be created within the QD SAM by using different types of quantum dots.

Different material and size quantum dots absorb at different wavelengths [21]. Regardless of material-set, when similarly sized QDs are spun during the stamping process, they will theoretically disperse based on ratio. Therefore, if we ablate a multi-material size-monodisperse QD SAM using a laser that only one of the two QD materials absorbs, then a pattern of holes within the QD SAM will be present.

At this point, we look back to the QD shadowmasking procedure listed in Chapter 6. Even though the RIE will etch away the organic and allow the dots to sinter, the produced periodic holes in the QD SAM should be large enough for a reactive species to penetrate and etch, if even for a few seconds. The dot layer can then be removed with a piranha etch, leaving a periodically nano-patterned substrate.

8.2 Process

Mix a solution of material A QDs (QDA) and combine with solution of material B QDs (QDB). The only restriction placed on QDA and QDB is that they both be relatively similar in size. The degree of size similarity is determined by the experimenter's need for long range order in the QD SAM. Spin and stamp the QDA-QDB solution onto silicon.

We now look to ablate one of the QD materials from the surface of the silicon. A wavelength and power must be chosen so that the quantum dot "particulates" on silicon are destroyed without affecting the silicon surface beyond the needs of the experiment. To accomplish this, the peak absorption wavelengths for QDA and QDB must be determined. We then choose a wavelength between these two absorption peaks, so that only one of the QD materials is ablated off the silicon surface. While the wavelength chosen should be lower energy than the peak absorption wavelength of silicon (264nm), it is best to keep the laser fluence below .2 J/cm^2 to avoid melting or possibly ablating the silicon [39]. Once the power and wavelength are finally determined, the laser is scanned over the entire surface of the sample.

At this point, a sub-pattern of holes should be present within the QD SAM. We now follow the RIE portion of the QD shadowmasking process in Section 6.2. The QD SAM is then removed with a piranha solution. A periodic pattern of holes should now exist in the silicon substrate.

8.3 Experimental Results and Discussion

As stated in the procedure, experimentation must be performed to determine the threshold that would remove QDs while not affecting silicon. Our QDA solution absorbed at wavelengths greater than 800nm and our QDB solution absorbed in the visible spectrum. In order to ablate only QDA while not damaging silicon, an 800nm infrared laser was used for all experiments. Laser fluence (as determined by spot size) was controlled by adjusting the distance between the sample to be ablated and a focusing lens. The lens to sample distance was controlled by an optics stage. As fine as 1mm adjustments were made to determine the threshold for ablating the QDs without affecting silicon. A 200mm focal length convex lens was used.

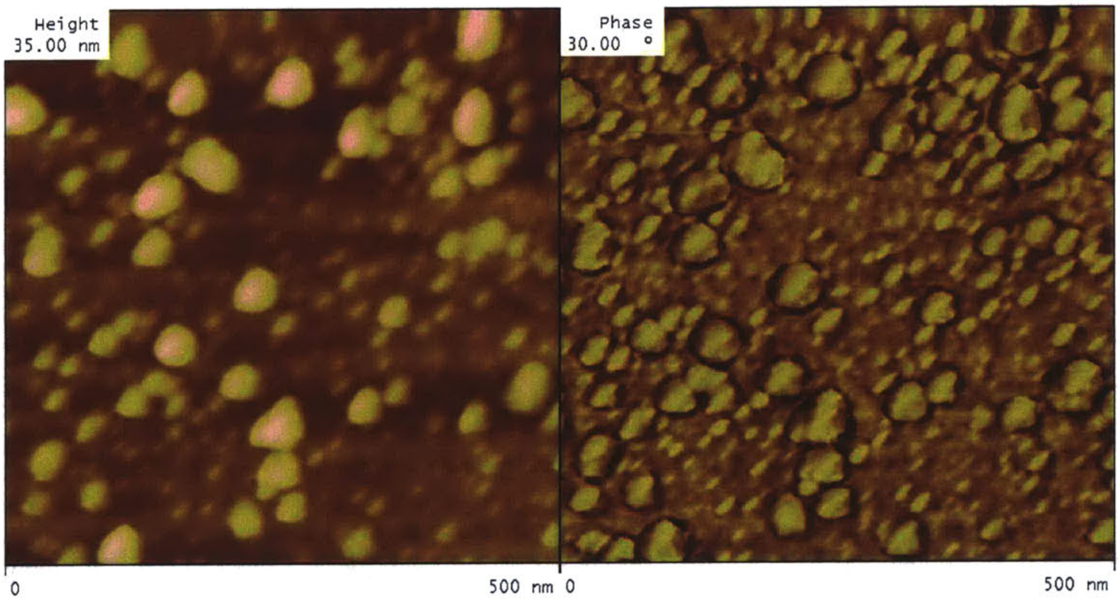

Figure 8-1: An AFM image of a PbSe QD SAM on Si after ablation with an 800nm laser.

At lens-sample spacings less than approximately 12mm, both the QD SAM and silicon substrate were damaged, as shown in Figure 8-1. Refer to pages 49, 50 & 51 for images of a stamped QD SAM before any processing is performed. At a lens-sample spacing greater than 12mm, the samples can visually be inspected to see that the "colored film" (the QD SAM) seems to be removed from the substrate, without having burned the silicon. Upon further inspection in an AFM, lens-sample spacings

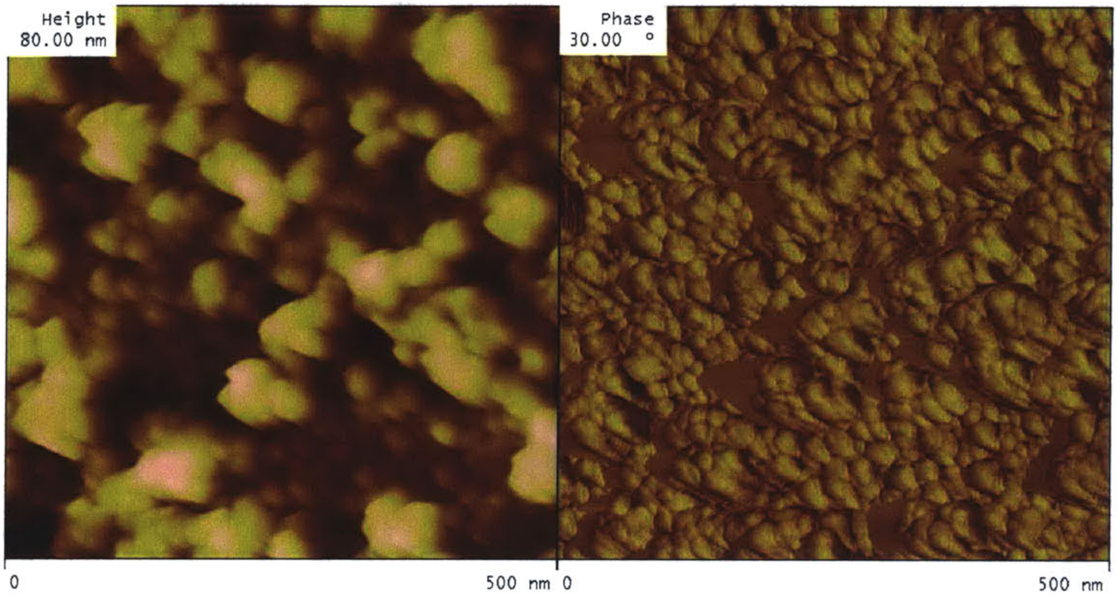

Figure 8-2: An atomic force micrograph of si altered by a highly focused 800nm laser.

between 12mm and 35mm (the maximum spacing attempted) produce samples with globules of material on their surface, imaged in Figure 8-2.

Despite further tunings of the lens-sample spacing, it was never apparent that the QDs were ablated without altering the silicon surface. Since a repeatable method of ablating solely the PbSe QDs without damaging the silicon could not be determined, we were forced to end our experimentation with selective QD ablation.

8.4 Conclusion

Laser ablation presents us with a selective method of sub-patterning a mixed material QD SAM. The process of achieving this sub-patterning is laid out in Section 7.2. Currently it is unknown why globules of presumably ablated, sintered and redeposited PbSe form until the threshold when silicon too is damaged. Due to restricted time and access to the laser ablation facilities, the author was unable to continue with the necessary experimentation needed to determine why the process did not work as expected. Thus laser ablation remain a possible means of achieving our patterning goals.

Chapter 9

Nano-Imprinting: Stamping[2]

In the previous three chapters, we have discussed various methods of patterning silicon on the nanometer scale using a quantum dot self-assembled monolayer template. In each case, patterning could not be achieved due to our inability to selectively remove a certain material or because the quantum dot cores and caps were too reactive. In this chapter, we proposed a method of patterning that exposes the QD SAM template to *no reactive species.*

9.1 Introduction

As based on previous work, Krishnan *et al* [40] have used imprints in the surface of aluminum to create varying size and arrangement pores during the anodization of aluminum. There are several methods of setting imprints or guiding the aluminum to form patterns of predetermined size pores. One method involves using colloidally grown crystals between 150nm and 500nm to form imprints in the aluminum surface [41]. We look to expand upon this research by using our 2 to 20nm quantum dots arranged in a self-assembled monolayer as a means of imprinting aluminum. As anodized alumina is more resilient to etching steps than QD SAMs, it could possibly serve as a hard mask for patterning any substrate [42].

9.2 Process

As described in Chapter 5, a QD SAM is stamped onto a substrate. We then thermally evaporate[1] aluminum onto the surface of another substrate. These two substrates are then pressed together with pressures ranging between 1000-2500 kg/cm^2 [43, 44] so that an imprint is formed in the aluminum surface.

At this point in the process, an imprint has been made on the surface of the aluminum, so we now need to utilize that imprint to make pores. The next step then is to anodize the aluminum sample[2]. The result is an aluminum oxide film with pores corresponding to the size and arrangement of the QD SAM.

We then RIE the anodized alumina sample. The ions of the RIE should pass through the pores of the aluminum oxide and etch the substrate below. Once the etch is completed, we remove the aluminum oxide from the substrate. A substrate with patterned nanometer holes remains.

As an alternative to utilizing the porous alumina as an RIE etch mask, the anodized alumina film can be employed as an electroplating template. If our silicon substrate is highly doped (and thus conductive) or if a conductive wetting layer is deposited under the aluminum film, metal can be electrodeposited within the alumina pores [46, 47]. The electrodeposition will result in metal rods with length depending on the thickness of the porous alumina film and the electroplating duration. The anodized alumina can then be etched away to release free-standing metal rods. In turn, the metal rods can serve as a resilient etch mask or even isolated points of charge storage.

These two porous alumina templating techniques are analogous to a lithographic photomask which can be utilized to produce two inverse patterns on a substrate. While the mask is the same, the resultant pattern depends on the type of photoresist spun on the substrate. The same is true in our case, except instead of different photoresists, we have different methods of manipulating our anodized alumina. If we

---

[1] Refer to Section 7.1.1 for a description of the thermal evaporation process.

[2] If you wish to understand the details of the aluminum anodization process, please refer to references [45] and [43].

use the anodized alumina film as a mask for an RIE etch, we can create nano-holes in our substrate. If we use the anodized alumina film as a template for creating free-standing metallic nano-rods, the nano-rods can serve as our etch mask and nano-rods of our substrate material will result. The power of these two methodologies lie in the fact that the two patterns created are both set by the initial QD SAM imprint.

9.3 Experimental Results

The substrates used for experimentation were half inch silicon squares with a layer of approximately 100nm of silicon oxide. Following the procedure listed above, a QD SAM was stamped onto one substrate and aluminum was thermally evaporated onto another. The two were then pressed together at pressures ranging from 2500 to 5000 pounds. This step has resulted in both aluminum imprinting, shown in Figure 9-1, and dot transfer, shown in Figure 9-2.

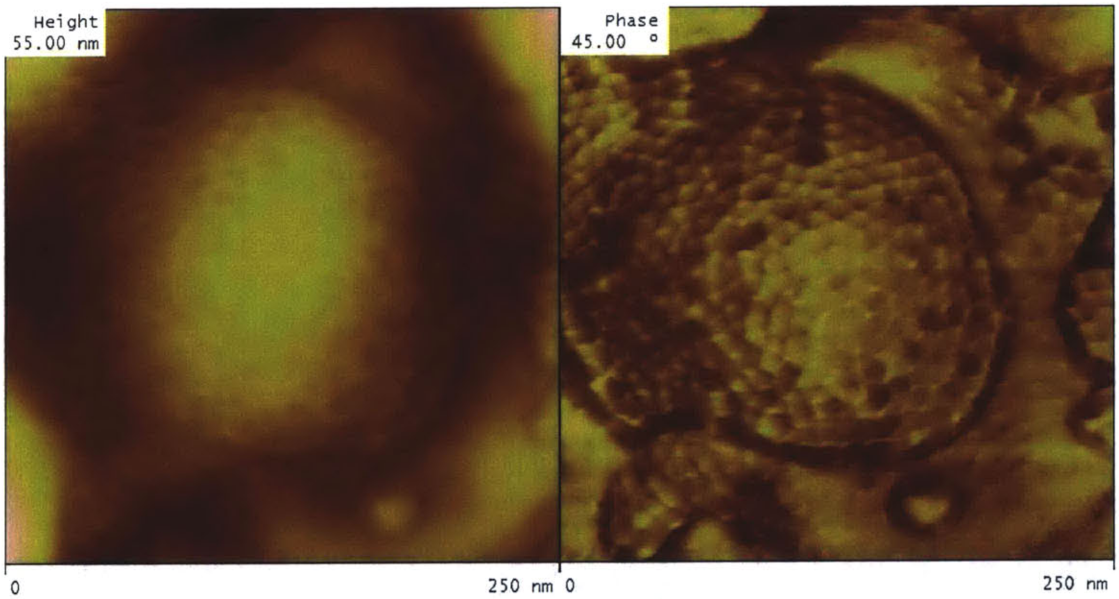

Figure 9-1: An atomic force micrograph of an imprinted aluminum film. The imprint was made using a QD SAM on silicon and 2500 pounds of force.

As long as either imprinting or dot transfer occurred, the samples were anodized. Figure 9-3 demonstrates the effect of anodization on an imprinted 110nm aluminum

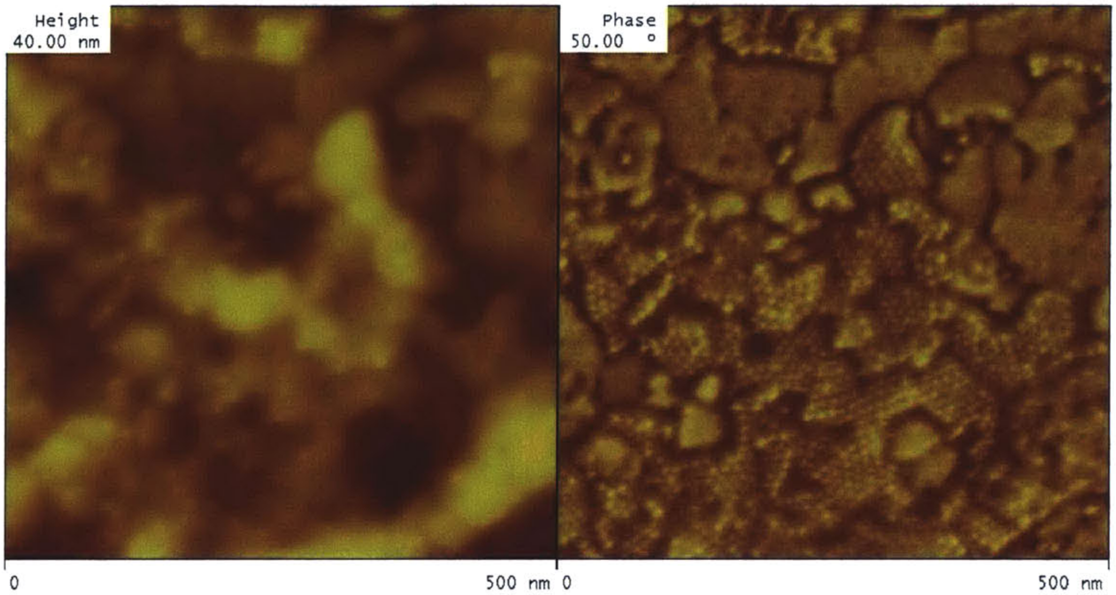

Figure 9-2: An AFM image of a PbSe QD SAM that has transfered from a silicon oxide substrate to an aluminum film.

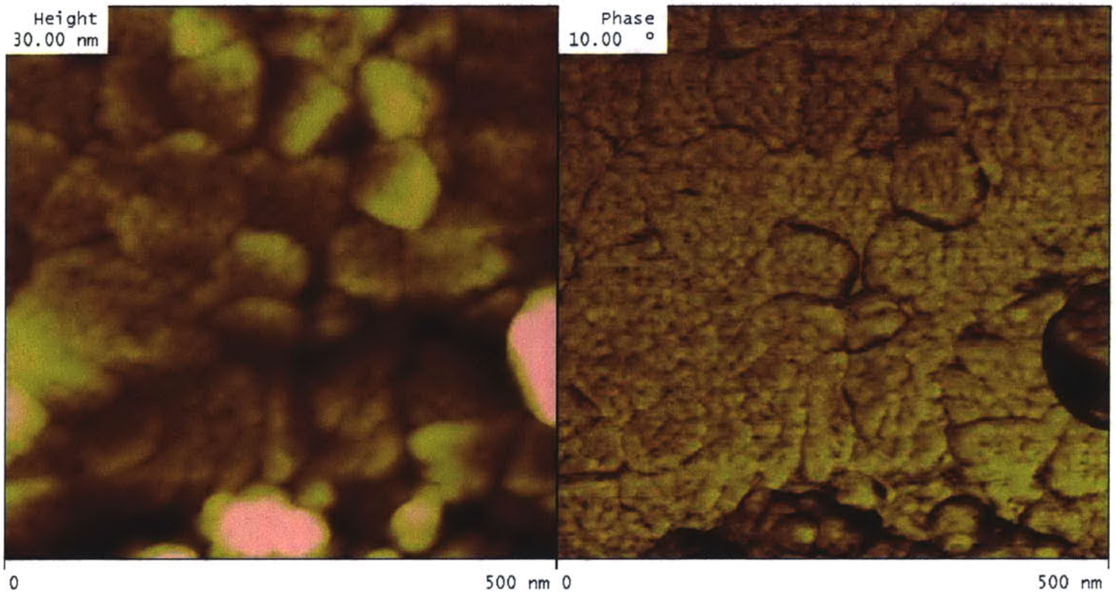

Figure 9-3: An atomic force micrograph of a porous 110nm aluminum oxide film after being imprinted with a QD SAM and then anodized at 5V.

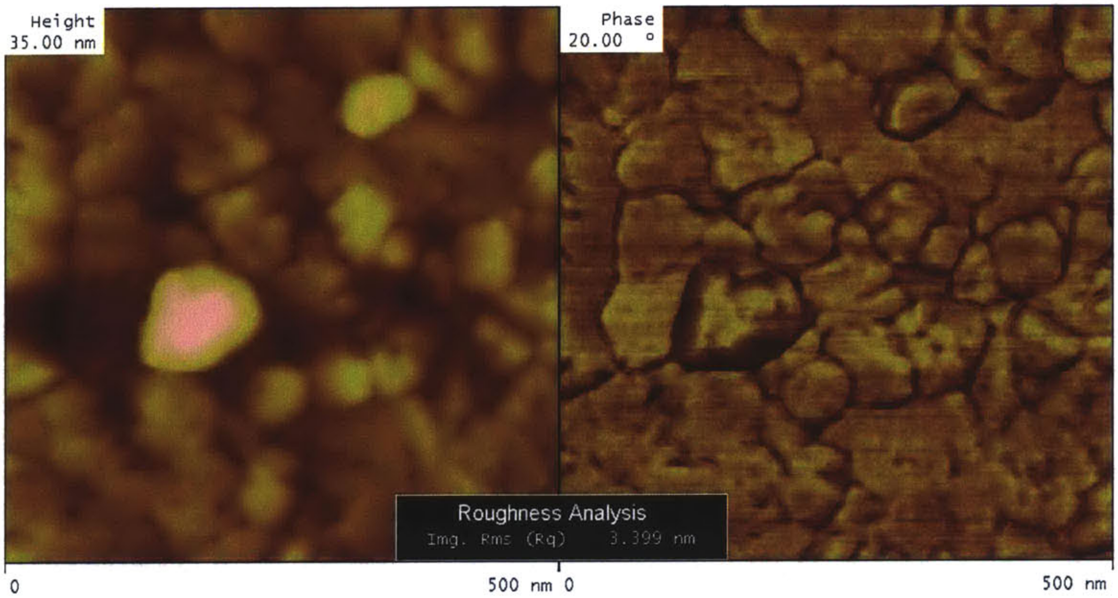

Figure 9-4: An AFM image with inset roughness analysis of a 110nm aluminum film before any imprinting or processing steps. RMS roughness noted accounts for the planar regions of the film.

film. This is contrasted with Figure 9-4, which is the surface of the aluminum before any processing steps. To further contrast the blank aluminum, Figure 9-5, a 3D computer rendering of the porous anodized alumina based on AFM height data, is presented.

Figure 9-5 illustrates that we have an aluminum film with approximately 8nm pores dispersed throughout it. The next step is to use the aluminum oxide film as a hard etch mask. Thus we RIE the sample using a gas that will selectively etch silicon oxide over aluminum oxide. While this step will be completed, time limitations prevented this step from occurring before the submission of this thesis. While we expect the anodized alumina to function as a successful etch mask, issues inherent to the RIE step are discussed in the following section.

9.4 Discussion

It is apparent that the procedure listed in Section 9.2 resulted in an aluminum oxide film with pores on the order of the size of the quantum dots used. What is not

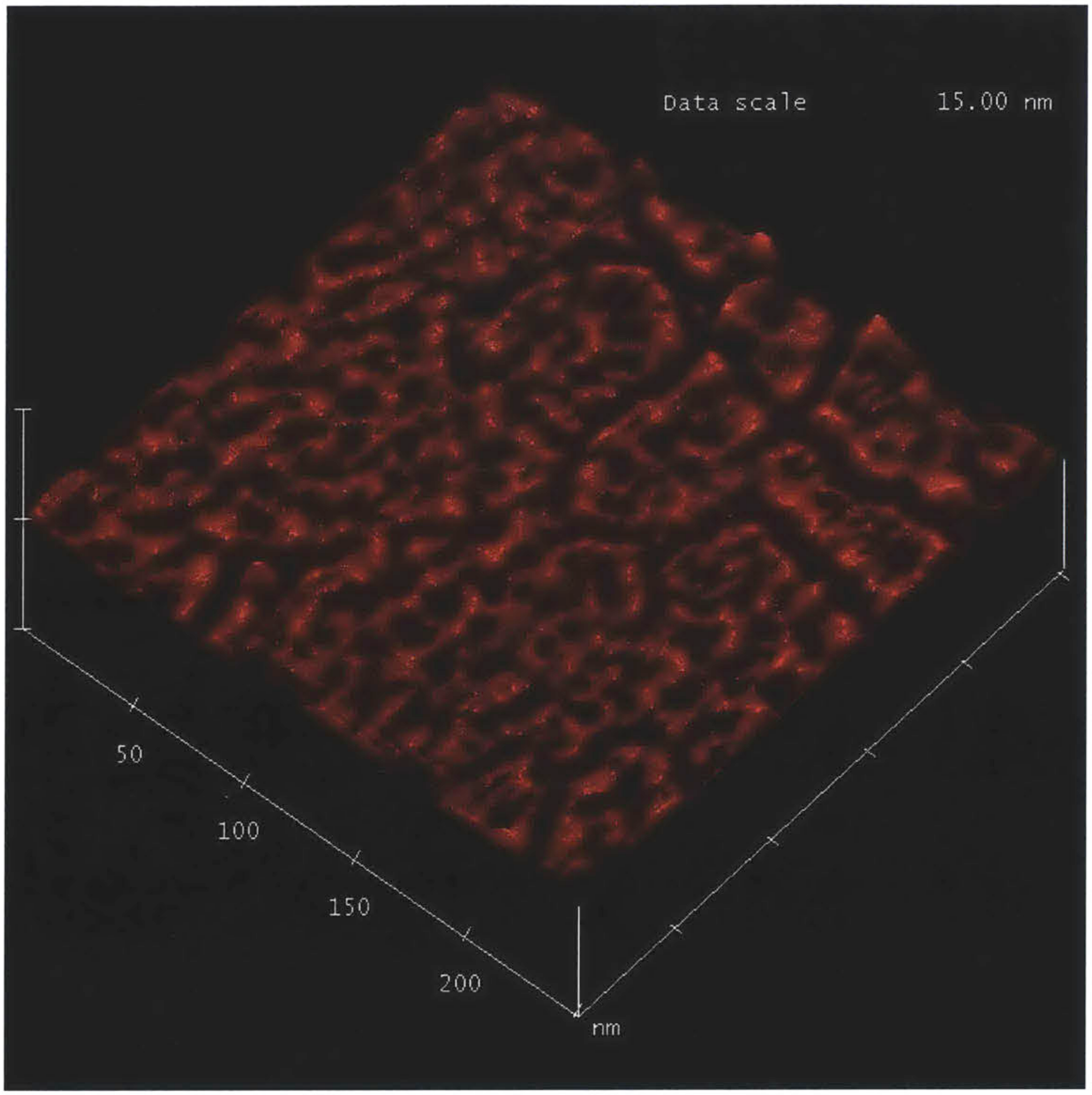

Figure 9-5: A 3D computer rendering of the anodized alumina surface based on AFM height data. The width and depth are 250nm and the height scale is 15nm. Note the holes over the entire film surface. Each hole is approximately 8nm - roughly the size of the quantum dots used for imprinting.

apparent is the hexagonally close-packed structure of the QD SAM. We propose that periodicity is not abundantly apparent because the aluminum film used is not flat enough for the needs of our procedure. Normally a film with 3nm of roughness is smooth enough for any application. In our case, that roughness, while smooth, does not reflect the high degree of granularity of the aluminum film. Not only are there many grains, but the grains are of small dimensions and different orientations. These features of the grains make it difficult to observe hexagonally close-packing of the pores. Figure 9-6 clearly illustrates this difficulty. There we see many very clear pores dispersed throughout the aluminum oxide surface. A few of the pores are even on a relatively large grain, which is boxed off in the lower right hand corner of the image. On that grain, we see pores spaced in a curved line, just as we would see QDs arranged in a SAM. Nonetheless, the grain is too narrow to decipher clear hexagonal close-packing. A smooth large-grain aluminum film is needed. A variety of techniques exist to smooth out the initial aluminum film - from varying deposition parameters to chemical mechanical polishing post-deposition [48].

In addition to smoothing of the aluminum film, the RIE process needs to be considered. Aluminum is a suitable mask material when using CF_4 to etch silicon oxide. Nonetheless, aluminum oxide, the material created during the anodization process, is not a fitting mask, as it will be etched away by CF_4. Therefore additional processing steps are necessary to either procure a gas that will selectively etch silicon oxide over aluminum oxide or to modify the aluminum oxide to become resilient to a CF_4 etch. Thankfully, aluminum oxide can be crystallized, which gives it the needed CF_4 resiliency [44]. Another factor to consider is gas flow and diffusion during the RIE process. As described in Section 6.1.1, a reactive species needs to reach the surface, react with it and then flow back into the gas. Only a limited number of reactive species, gases and particles can flow through a 8nm-wide and 110nm-long tunnel, such as the pores present on our samples. To expedite the RIE step, the aluminum film needs to be made as thin as possible. Otherwise, etching will become the time-limiting step in our procedure.

Wet etching should not be considered as an alternative. Just as with gases, liquid

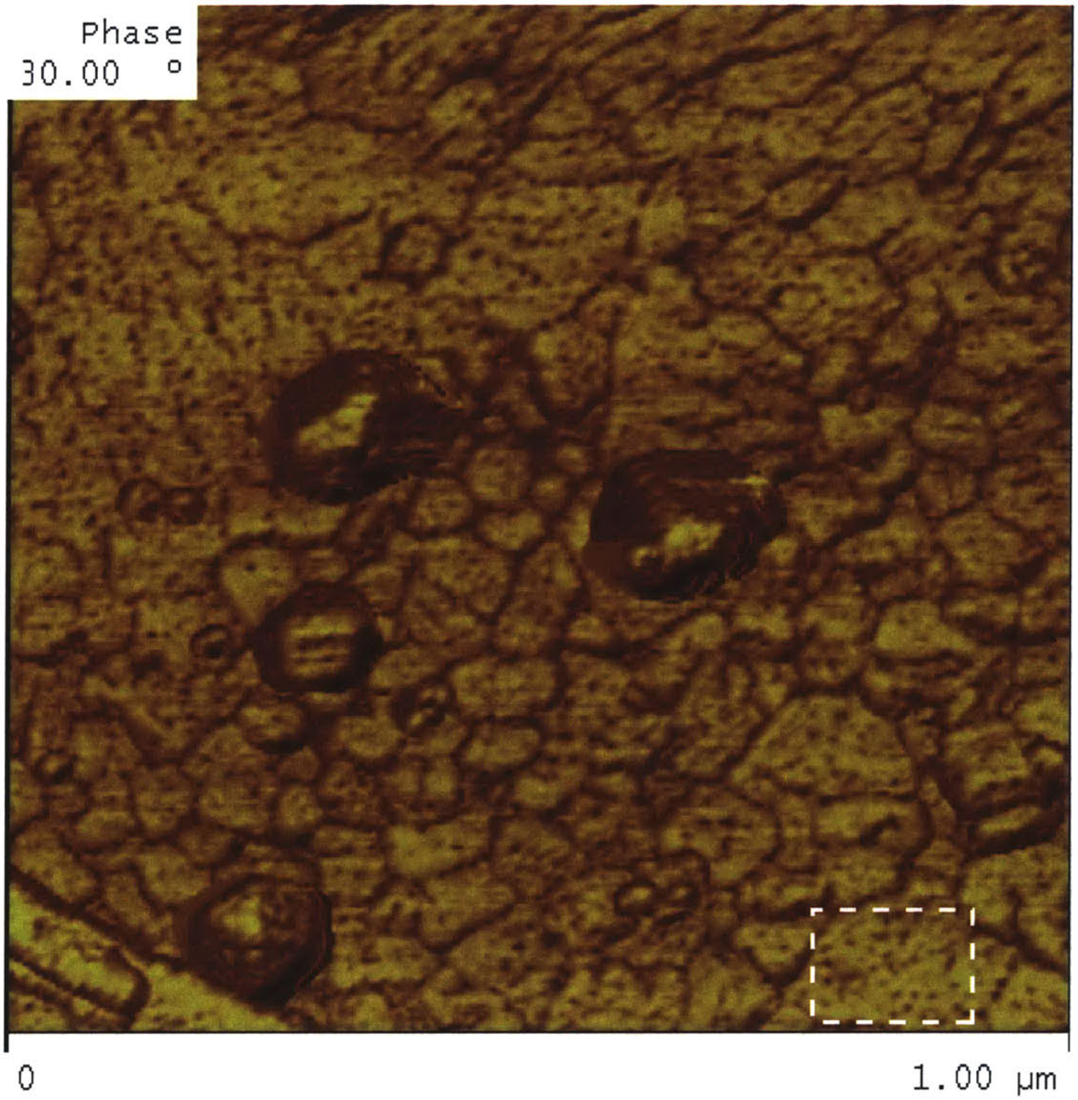

Figure 9-6: An atomic force micrograph of a porous 110nm aluminum oxide film as a result of imprinting with a QD SAM and then anodizing at 7V. The boxed area highlights an arrangement of pores with size and spacing similar to a QD SAM.

flow through the small pores is limited. In addition, the best anisotropic wet etch will not retain 8nm features. A dry anisotropic etch is the only option. Thus the above considerations for RIE must be solved.

Admittedly, there a few hurdles to overcome before we can pass our desired pattern into silicon. Nonetheless, it is appropriate to note that this work has produced the smallest imprint-based anodized alumina pores known. Note that the size of these pores can be controlled by varying the size of the quantum dots used to imprint the aluminum. In addition, when used an etching mask, these size-tunable pores are the basis for the ability to pattern any material in the 2 to 20nm range.

9.5 Conclusion

In this section, we present a method for nano-patterning by imprinting and anodizing an aluminum film. We then show that this procedure results in a successful pattern of 8nm pores. We also lay out the final steps and considerations needed to fulfill the goal of patterning a silicon substrate in the 2 to 20nm range.

Chapter 10

Discussion

Patterning of images has been a goal of man throughout time. Developments and accomplishments in patterning have occured through to present day. Modern patterning can be classified into two types: top-down and bottom-up. Top-down, the primary type of patterning, creates small patterns from a larger "bulk" substrate. Modern semiconductor processing techniques, including optical and focused beam lithography, are examples of top-down patterning. Bottom-up patterning, a more recent development, is accomplished through a large-scale organization of molecules and atoms. While each method is powerful in its own right, the ultimate ability to quickly and reliably pattern is limited to outside the 2 to 20nm range.

By using large-scale self-assembled size-tunable molecular arrangements and bulk substrate processing techniques, the research presented in this thesis combines the best features of top-down and bottom-up patterning. Of course, there are difficulties with our processes. Most of the difficulties stem from the chemical reactivity of the nanocrystals used in our self-assembled patterning template. Nonetheless, a method of patterning in which the nanocrystals are isolated from other chemically reactive species is presented and shown to have promising results. As a result, we now possess the tools needed to bridge the 2 to 20nm range of patterning.

Chapter 11

Conclusion

In this thesis we have explored the use of a self-assembled nanocrystal monolayer as a template for patterning in the 2 to 20nm range. There has been previous work done to pattern near 20nm using colloidally-grown nanocrystals [49] and block co-polymers [50]. The research in this thesis expands upon that work, showing that nanocrystals can be used to make patterns well below the 20nm mark with a well-defined periodicity previously unattained. Now that we have outlined in this thesis the processes which result in a sub-20nm periodic pattern, we look to improve upon them. There are many modifications that can be made at every stage to make 2 to 20nm patterning more reliable, easier and faster.

As mentioned previously, the nanocrystals used in this thesis work, organic-capped lead selenide dots, are a chemically reactive species which readily sinters. If chemists can produce nanocrystals that withstand various patterning techniques, most notably a reactive ion etch with CF_4 gas, then Chapter 6's QD Shadowmasking would present an expedient alternative to Chapter 9's Nano-Imprinting. If the nanocrystals produced also lack a capping layer, then Chapter 7's QD Lift-Off technique becomes another solution.

While altering the material set avails some other possibilities, there are many more patterning techniques that can be attempted with the current PbSe QD SAMs. It is currently unknown what type of interaction exists between the PbSe core and silicon's native oxide. If there is even a basic Van der Waals bond between the two materials, the dots could be used as a patterning initiator. An example of this is a KOH etch of silicon. The fact that KOH only etches along the (111) plane of silicon has been used to create inverted pyramids in silicon [51]. If a bond between QD and silicon is present, it may act as an etch starting point for KOH, resulting in inverted pyramids on the scale of the periodicity of the QDs. Another example is electroplating a QD-SAM-on-silicon sample. Again, if there is a bond between QD and silicon, electroplated metal may only form between QDs. This electroplated metal may then serve as a basis for more chemically reactive patterning methods.

PDMS has already been used to retain and then transfer 100nm patterns [52]. In Section 5.2, we showed that PDMS has a roughness on the order of half a nanometer over 9 square microns. That order of roughness should allow 2 to 20nm imprints to be distinguished throughout the PDMS surface. Thus if PDMS were cured on a QD SAM on silicon surface, the QD SAM pattern should be retained by the PDMS. This PDMS "master" could then be used to imprint other surfaces or be used as a method of depositing material from the master imprint to the surface of another substrate.

All of these future patterning techniques depend on methods of depositing a QD SAM. Chapters 4 & 5 discussed different processes of forming and depositing QD SAMs. These processes too can be improved. As mentioned in Section 5.2, different solvents have different viscosities and evaporation rates. When spin-casting or stamping, these differing solvent properties result in QD SAMs with different size grains, organizations and stacking. It is thus evident that more research needs to be done into the effects of using different solvents and solvent mixtures, most notably a mixture of chloroform and cholorobenzene.

Other modifications can be made to the stamping process as well. PDMS and parylene have worked very well for stamping, as illustrated in Chapter 5, but the multi-step process in creating stamps generates variability in results. A conformable material that is wet by a QD solvent would be an ideal replacement for the parylene-coated PDMS cubes. In addition, much of the variability from stamping occurs during the final manipulation of the PDMS and the stamping press, both of which are now controlled manually. Currently, the Laboratory of Organic Optics and Electronics at

MIT is working on a more automated method of stamping. Nevertheless, continued work is needed to make stamping as consistent and reproducible as possible.

While this thesis work underscores the need for new quantum dot structures, improved solvent mixtures & enhanced mechanisms of depositing QD SAMs, our data also attests to the promising capabilities of the existing technology. Through the research presented in Chapter 9, we already see that patterning in the 2 to 20nm range is very much possible. While this is the first imprint-based patterning data ever presented on this size scale, there is tremendous potential for the templating techniques presented in this thesis to pattern any substrate at any resolution desired.

Appendix A

Analytical Solution for the Time-Independent Schrödinger Equation

We first refer to Equation 2.1 - the time-independent Schrödinger equation:

$$E\psi(x) = -\frac{\hbar^2}{2m}\frac{\partial^2}{\partial x^2}\psi(x),$$

where E represents the energy of the QP, $\hbar$ is Planck's constant divided by 2π, m is the mass of the particle and $\psi(x,t)$ is the wavefunction of the particle.

Divide both sides by $-\frac{\hbar^2}{2m}$ to obtain

$$-\frac{2mE}{\hbar^2}\psi(x) = \frac{\partial^2}{\partial x^2}\psi(x).$$

Let

$$K \equiv \frac{\sqrt{2mE}}{\hbar}.$$

The equation then becomes

$$-K^2\psi(x) = \frac{\partial^2}{\partial x^2}\psi(x).$$

The above differential equation is solved when $\psi(x)$ takes on the form

$$\psi = Ae^{iKx} + Be^{-iKx}, \tag{A.1}$$

where A & B vary based on particle-well interaction. Using Euler's equation[1], Equation A.1 becomes

$$\psi = A \sin Kx + B \cos Kx,$$

where A & B are different particle-environment interaction coefficients than those in Equation A.1.

To find the solution within the walls of a quantum well, we change E to $V_0 - E$, where V_0 is the potential height of the well. Instead of K, we have

$$Q \equiv \frac{\sqrt{2m(V_0 - E)}}{\hbar}.$$

Using Q, the resultant equation becomes

$$Q^2\psi(x) = \frac{\partial^2}{\partial x^2}\psi(x).$$

The resultant solution for $\psi(x)$ thus has the form

$$\psi = Ce^{Qx} + De^{-Qx}, \tag{A.2}$$

where C & D vary based on particle-well interaction. Equation A.2 can be represented with a summation of sinh and cosh expressions. For convenience, the sum of exponentials are used in our calculations.□

---

[1] $e^{ix} = \cos x + i \sin x$

Appendix B

Analytical Solution for the Finite Potential Well

Solving for the finite potential requires that the particle wavefunction is continuous at the boundaries of the well. We thus need to use Equations 2.2 & 2.3:

$$\begin{array}{ll} \psi_I(-\frac{a}{2}) = \psi_{II}(-\frac{a}{2}) & \frac{\partial \psi_I(-\frac{a}{2})}{\partial x} = \frac{\partial \psi_{II}(-\frac{a}{2})}{\partial x} \\ \psi_{II}(+\frac{a}{2}) = \psi_{III}(+\frac{a}{2}) & \frac{\partial \psi_{II}(+\frac{a}{2})}{\partial x} = \frac{\partial \psi_{III}(+\frac{a}{2})}{\partial x} \end{array}$$

In Equation 2.4, we defined area II to have the wavefunction

$$\psi_{well} = Ae^{iKx} + Be^{-iKx}.$$

We also defined areas I & III to be of the form

$$\psi_{well} = Ce^{Qx} + De^{-Qx}$$

in Equation 2.6. For clarity, let area I's wavefunction be

$$\psi_I = Ce^{Qx} + De^{-Qx}$$

and area II's wavefunction be

$$\psi_{III} = Fe^{Qx} + Ge^{-Qx}.$$

To see a derivation of these equations and their terms, refer to Appendix A.

Examining ψ_I & ψ_{III} further, we see that both contain exponentials that approach infinity as distance from the well is increased. Since energy can not approach infinity, we set

$$C = 0$$

$$F = 0$$

and are left with

$$\begin{aligned} \psi_I &= De^{-Qx} && \text{(B.1)} \\ \psi_{III} &= Ge^{-Qx}. && \text{(B.2)} \end{aligned}$$

We introduce Equations 2.4 & B.1 into Equation 2.2 at $x = -\frac{a}{2}$ - the boundary between area I and area II according to Figure 2-1 - to yield

$$\begin{aligned} -A\sin K\frac{a}{2} + B\cos K\frac{a}{2} &= Ce^{-Q\frac{a}{2}} && \text{(B.3)} \\ AK\cos K\frac{a}{2} + BK\sin K\frac{a}{2} &= CQe^{-Q\frac{a}{2}}. && \text{(B.4)} \end{aligned}$$

Then plug Equations 2.4 & B.2 into Equation 2.3 at $x = \frac{a}{2}$ - the boundary between area II and area III - to yield

$$\begin{aligned} A\sin K\frac{a}{2} + B\cos K\frac{a}{2} &= Ge^{-Q\frac{a}{2}} && \text{(B.5)} \\ AK\cos K\frac{a}{2} - BK\sin K\frac{a}{2} &= -GQe^{-Q\frac{a}{2}}. && \text{(B.6)} \end{aligned}$$

Through linear combinations of B.3 through B.6, we attain the following series of equations:

$$\begin{aligned}
2B\cos K\frac{a}{2} &= (C+G)e^{-Q\frac{a}{2}} && \text{(B.7)}\\
2A\sin K\frac{a}{2} &= (G-C)e^{-Q\frac{a}{2}} && \text{(B.8)}\\
2AK\cos K\frac{a}{2} &= Q(C-G)e^{-Q\frac{a}{2}} && \text{(B.9)}\\
2BK\sin K\frac{a}{2} &= Q(C+G)e^{-Q\frac{a}{2}}. && \text{(B.10)}
\end{aligned}$$

Analyzing these equations, $B \neq 0$ when $(G+C)=0$ and $A \neq 0$ when $(G-C)=0$. Therefore we break these into two cases. First, given $B=0$ and $(G+C)=0$, Equation B.10 divided by Equation B.7 is

$$K\tan K\frac{a}{2} = Q. \tag{B.11}$$

Then, given $A=0$ and $(G-C)=0$, Equation B.9 divided by Equation B.8 is

$$K\cot K\frac{a}{2} = -Q. \tag{B.12}$$

Adding Equations B.11 and B.12, we attain

$$K[\tan K\frac{a}{2} + \cot K\frac{a}{2}] = 0,$$

which can be rearranged to

$$\tan^2 K\frac{a}{2} = -1.$$

Since the tangent of a value can never be imaginary, the cases where $B=0$ when $(G+C)=0$ and $A=0$ when $(G-C)=0$ can not occur at the same time. Therefore we analyze these as two separate cases.

In the first case, $A \neq 0$, $(G - C) \neq 0$, $B = 0$ & $(G + C) = 0$, which means $G = -C$. This modifies Equation B.8 to become

$$G = A \sin K\frac{a}{2}\, e^{Q\frac{a}{2}}. \tag{B.13}$$

Using our case definition, Equation B.13 and our wavefunctions 2.4, B.1 & B.2, we obtain the following solutions:

$$\begin{aligned}
\psi_I &= [-A \sin K\tfrac{a}{2}\ e^{Q\frac{a}{2}}]\ e^{Qx} && x \leq -\tfrac{a}{2} \\
\psi_{II} &= [A] \sin Kx && -\tfrac{a}{2} \leq x \leq \tfrac{a}{2} \\
\psi_{III} &= [A \sin K\tfrac{a}{2}\ e^{Q\frac{a}{2}}]\ e^{-Qx} && x \geq \tfrac{a}{2}.
\end{aligned}$$

In the second case, $B \neq 0$, $(G + C) \neq 0$, $A = 0$ & $(G - C) = 0$, which means $G = C$. This modifies Equation B.7 to become

$$C = B \cos K\frac{a}{2}\, e^{-Q\frac{a}{2}}. \tag{B.14}$$

Using our case definition, Equation B.14 and our wavefunctions 2.4, B.1 & B.2, we obtain these solutions:

$$\begin{aligned}
\psi_I &= [B \cos K\tfrac{a}{2}\ e^{Q\frac{a}{2}}]\ e^{Qx} && x \leq -\tfrac{a}{2} \\
\psi_{II} &= [B] \cos Kx && -\tfrac{a}{2} \leq x \leq \tfrac{a}{2} \\
\psi_{III} &= [B \cos K\tfrac{a}{2}\ e^{Q\frac{a}{2}}]\ e^{-Qx} && x \geq \tfrac{a}{2}.
\end{aligned}$$

Now that we have the wavefunctions for the two cases, we need to solve for K & Q. This is done by multiplying Equation B.12 by $\frac{a}{2}$ and substituting in the definitions of K (Equation 2.5) and Q (Equation 2.7) to obtain

$$\sqrt{\frac{mEa^2}{2\hbar^2}} \tan\sqrt{\frac{mEa^2}{2\hbar^2}} = \sqrt{\frac{m(V_0 - E)a^2}{2\hbar^2}}.$$

Let

$$\varepsilon \equiv \sqrt{\frac{mEa^2}{2\hbar^2}}.$$

Therefore we have

$$\varepsilon \tan \varepsilon = \sqrt{\frac{mV_0a^2}{2\hbar^2} - \varepsilon^2},$$

where we define the left hand side to be $\rho(\varepsilon)$ and the right hand side to be $q(\varepsilon)$. The values of ε that allow $\rho(\varepsilon)$ to equal $q(\varepsilon)$ are the allowed discrete energy values, or eigenvalues, of the finite potential well system.□

Appendix C

Kronig-Penney Simulation Matlab Code [KronigPenneyModel.m]

Below is KronigPenneyModel.m, the Matlab code for the simulations in Section 2.4. The function KronigPenneyDifMin.m referred to in this code appears in Appendix D. Parts of code are based on Conor Madigan's work [53], as noted.

```
%KronigPenneyModel.m
%     A script to solve the Kronig Penney Model.
%Copyright Ryan Tabone MMV
clear all;

%_VARIABLES_ (MKS):
eV = 4.7; %Potential in eV; Si Work Function = 4.7eV
    %n+ = 4.1eV; p+ = 5.2eV
U = eV*1.6e-19; %Energy converted from eV to Joules
a = 9e-9; %Size of well in meters
b = 6e-9; %Size of spacing between wells in meters
En = 1e-19;
num_bands = 3; %Number of bands to compute. To compute all bands in
```

```
%interval, comment this line out and uncomment num_bands
%definition further along in the code.

%_CONSTANTS_ (MKS):
m = (0.36)*9.10938188e-31; %Effective mass of an electron in Si in kg
%holes are .81
h_bar = 1.05e-34; %in Joule-seconds

%Additional Definitions - Based on Conor Madigan’s work.
K_range = (2*num_bands)*pi; %relatively arbitrary setpoints for sin/cos
K_plot = (-K_range:0.1:K_range)/(a+b); %Divide by a+b, the period of the interval
energy_eigenv = h_bar^2 * K_plot.^2 / (2*m); %By definition
Q_plot = sqrt(2*m*(U-energy_eigenv)) / h_bar;
lhs = ((Q_plot.^2 - K_plot.^2) ./ (2*Q_plot.*K_plot)) .* sinh(Q_plot*b) .* sin(K_plot*a)
+ cosh(Q_plot*b)
.* cos(K_plot.*a);

%Second Plot based on Conor’s method.
figure(2);
clf;
grid on;
hold on;
title(’Kronig-Penney Plot’)
xlabel(’cos k(a+b)’)
ylabel(’[(Q^2 - K^2)/2QK] sinh(Qb) sin(Ka) + cosh(Qb) cos(Ka)’)
plot(K_plot, lhs);
hold off;

%Find sign changes (i.e. zero points) in lhs plot
lhs_length = length(lhs);
```

```
K_zero_index = 1;
for (s = round(lhs_length/2):1:lhs_length)
if ((lhs(1,s-1) > 0) & (lhs(1,s) < 0)) — ((lhs(1,s-1) < 0) & (lhs(1,s) > 0))
K_zero_locations(1,K_zero_index) = s;
K_zero_index = K_zero_index + 1;
end
end


%Compute & plot the energy bands
k = 0:.01:1; %number of pi
figure(3);
clf;
hold on;
grid on;
title(’Energy vs. Wavenumber’)
xlabel(’K, in multiples of \pi ’)
ylabel(’Energy, in units of ((hbar^2)(\pi ^2))/2ma^2’)
options = optimset(’maxfunevals’, 1e4, ’maxiter’, 1e4, ’tolx’, 1e-4, ’tolfun’, 1e-4);
for (j = 1:1:num_bands)
K_zero = K_plot(1,K_zero_locations(1,j));
for (n = 1:1:length(k))
K_difmin(n) = fminsearch(’KronigPenneyDifMin’, K_zero, options, cos(k(n)*pi), a,
    b, m, U, h_bar);
energy_bands(j,n) = ((K_difmin(n))^2 * (a+b)^2) / (pi^2);
end
K_bands(j,:) = K_difmin;
Q_bands(j,:) = sqrt(((2*m)/(h_bar^2))*(U - (h_bar^2)*(K_difmin.^2)/(2*m)));


plot(k, energy_bands(j,:));
end
```

```
figure(4);
eb_length = length(energy_bands(1,:));
clf;
hold on;
title('Energy vs. Wavenumber')
xlabel('K, in multiples of \pi')
ylabel('Energy, in units of ((hbar^2)(\pi ^2))/2ma^2')
grid on;
for (j = 1:1:num_bands)
if (mod(j,2) == 1)
plot(k+j-1, energy_bands(j,:));
else
plot(j-k, energy_bands(j,:));
end
end

%%%%%%%%%%%%%%%%%%%%%%%%%%%%%%%%%%%%%%%%%%%%%%%%
% All code below based on Conor Madigan's Work %
%%%%%%%%%%%%%%%%%%%%%%%%%%%%%%%%%%%%%%%%%%%%%%%%
%Plot wavefunction
x1 = (-1:0.001:0)*(b);
x2 = (0:0.001:1)*(a);
xtotal = [x1 x2 (x1+(a+b))];
U_profile = [eV*ones(size(x1)) zeros(size(x2)) eV*ones(size(x1))];

psi1 = zeros(num_bands,length(x1));
psi2 = zeros(num_bands,length(x2));

for (n=1:1:num_bands)
```

```
K = K_bands(n,1);
Q = Q_bands(n,1);
T = [1 1 -1 -1; i*K -i*K -Q Q; exp(i*K*a) exp(-i*K*a) -exp(-Q*b) -exp(Q*b);
    i*K*exp(i*K*a) -i*K*exp(-i*K*a) -Q*exp(-Q*b) Q*exp(Q*b)];
f = null(T);
psi1(n,:) = f(3)*exp(Q*x1)+f(4)*exp(-Q*x1);
psi2(n,:) = f(1)*exp(i*K*x2)+f(2)*exp(-i*K*x2);
end

figure(7);
clf;
plot(xtotal,U_profile,'r', 'LineWidth', 2)
color = 'kbgmcy';
hold on;
title('Plot of \psi^2')
xlabel('m')
ylabel('\psi^2 [a.u.]')
for (n=1:1:num_bands)
plot(x1,2.5*abs(psi1(n,:)).^2,color(mod(n,7)));
plot(x2,2.5*abs(psi2(n,:)).^2,color(mod(n,7)));
plot(x1+(a+b),2.5*abs(psi1(n,:)).^2,color(mod(n,7)));
end
hold off;

%Plot two wavefunctions of two adjacent wells
xtotal_ext = [-1.001*b x1 x2 (x1+(a+b)) (x2+(a+b)) x1+2*(a+b) 2*(a+b)+.001*b];
U_profile_ext = [0 eV*ones(size(x1)) zeros(size(x2)) eV*ones(size(x1)) zeros(size(x2))
eV*ones(size(x1)) 0];

figure(8);
```

```
clf;

plot(xtotal_ext,U_profile_ext,'r', 'LineWidth', 2)
color = 'kbgmcy';
hold on;
title('Plot of \psi^2')
xlabel('m')
ylabel('\psi^2 [a.u.]')
for (n=1:1:num_bands)
plot(x1,2.5*abs(psi1(n,:)).^2,color(mod(n,7)));
plot(x2,2.5*abs(psi2(n,:)).^2,color(mod(n,7)));
plot(x1+(a+b),2.5*abs(psi1(n,:)).^2,color(mod(n,7)));
plot(x2+(a+b),2.5*abs(psi2(n,:)).^2,color(mod(n,7)));
plot(x1+2*(a+b),2.5*abs(psi1(n,:)).^2,color(mod(n,7)));
end
hold off;
```

Appendix D

Difference Minimization Matlab Code [KronigPenneyDifMin.m]

The following Matlab code is a function referred to by KronigPenneyModel.m, which is in Appendix C.

```
%KronigPenneyDifMin.m
%   A script used by KronigPenneyModel.m to minimize the difference
%   between the lhs and rhs of the Kronig-Penney Equation
%Copyright Ryan Tabone MMV

function SqrDif = KronigPenneyDifMin(K_zero, rhs, a, b, m, U_0, h_bar)

energy_eigenv = h_bar^2 * K_zero^2 / (2*m); %By definition [pg 180]
Q_zero = sqrt(2*m*(U_0 - energy_eigenv)) / h_bar;
lhs = ((Q_zero^2 - K_zero^2) / (2*Q_zero*K_zero)) * sinh(Q_zero*b) * sin(K_zero*a)
    + cosh(Q_zero*b) * cos(K_zero*a);

Dif = lhs - rhs;
SqrDif = Dif^2;
```

Bibliography

[1] Michael E. Walsh. *On the design of lithographic interferometers and their application.* Ph.d. thesis, Massachusetts Institute of Technology, 2004.

[2] W. F. Brinkman, D. E. Haggan, and W. W. Troutman. A history of the invention of the transistor and where it will lead us. *IEEE journal of solid-state circuits*, 32(12):8, 1997.

[3] M. Geissler and Y. Xia. Patterning: Principles and some new developments. *Advanced materials*, 16(15):22, 2004.

[4] G. E. Moore. Lithography and the future of moore's law. *SPIE milestone series*, 178:182–197, 2004.

[5] R. H. Stulen and D. W. Sweeney. Extreme ultraviolet lithography. *IEEE journal of quantum electronics*, 35(5):6, 1999.

[6] J.H. Klein-Wiele, J. Bekesi, and P. Simon. Sub-micron patterning of solid materials with ultraviolet femtosecond pulses. *Applied physics. A, Materials science & processing*, 79(4-6):775 – 778, 2004.

[7] D. Jang and D. Kim. Synthesis of nanoparticles by pulsed laser ablation of consolidated metal microparticles. *Applied physics. A, Materials science & processing*, 79(8):1985 – 1988, 2004.

[8] S. Matsui and Y. Ochiai. Focused ion beam applications to solid state devices. *Nanotechnology*, 7(3):247, 1996.

[9] F. Frost and B. Rauschenbach. Nanostructuring of solid surfaces by ion-beam erosion. *Applied physics. A, Materials science & processing*, 77(1):10, 2003.

[10] C. Vieu, F. Carcenac, A. Pepin, Y. Chen, M. Mejias, A. Lebib, L. Manin-Ferlazzo, L. Couraud, and H. Launois. Electron beam lithography: resolution limits and applications. *Applied surface science*, 164(1):7, 2000.

[11] D. M. Eigler and E. K. Schweizer. Positioning single atoms with a scanning tunneling microscope. *Nature*, 344(6266):524–526, 1990.

[12] Xiang Zhang, Cheng Sun, and Nicholas Fang. Manufacturing at nanoscale: Top-down, bottom-up and system engineering. *Journal of Nanoparticle Research*, 6(1):6, 2004.

[13] J. M. Lehn. Toward self-organization and complex matter. *Science*, 295(5564):2400–2403, 2002.

[14] T. Van Buuren, L. N. Dinh, L. L. Chase, W. J. Siekhaus, and L. J. Terminello. Changes in the electronic properties of si nanocrystals as a function of particle size. *Physical review letters*, 80(17):4, 1998.

[15] F. J. Himpsel, A. Kirakosian, J. N. Crain, J. L. Lin, and D. Y. Petrovykh. Self-assembly of one-dimensional nanostructures at silicon surfaces. *Solid state communications*, 117(3):149–157, 2001.

[16] V. M. Aroutiounian and M. Zh Ghulinyan. Electrical conductivity mechanisms in porous silicon. *Physica status solidi. A, Applied research*, 197(2):5, 2003.

[17] V. Ranjan, M. Kapoor, and V. A. Singh. The band gap in silicon nanocrystallites. *Journal of physics. Condensed matter: an Institute of Physics journal*, 14(Part 26):6647–6656, 2002.

[18] B. E. Kane. Silicon-based quantum computation. *Fortschritte der Physik*, 48(9):20, 2000.

[19] J. M. Depuydt, H. Cheng, J. E. Potts, T. L. Smith, and S. K. Mohapatra. Growth of undoped znse on (100) gaas by molecular-beam epitaxy: An investigation of the effects of growth temperature and beam pressure ratio. *Journal of Applied Physics*, 62(12):4756–4762, 1987.

[20] C. B. Murray, D. J. Norris, and M. G. Bawendi. Synthesis and characterization of nearly monodisperse cde (e = s,se,te) semiconductor nanocrystallites. *Journal of the American Chemical Society*, 115(19):8706, 1993.

[21] Al L. Efros and M. Rosen. The electronic structure of semiconductor nanocrystals. *Annual review of materials science*, 30:48, 2000.

[22] M. G. Bawendi, P. J. Carroll, William L. Wilson, and L. E. Brus. Luminescence properties of cdse quantum crystallites: Resonance between interior and surface localized states. *The Journal of chemical physics*, 96(2):946–954, 1992.

[23] B. O. Dabbousi, M. G. Bawendi, O. Onitsuka, and M. F. Rubner. Electroluminescence from cdse quantum-dot/polymer composites. *Applied physics letters*, 66(11):1316, 1995.

[24] C. R. Kagan, C. B. Murray, M. Nirmal, and M. G. Bawendi. Electronic energy transfer in cdse quantum dot solids. *Physical review letters*, 76(9):4, 1996.

[25] S. Coe-Sullivan, J. S. Steckel, W. K. Woo, M.G. Bawendi, and V. Bulovic. Large area ordered quantum dot monolayers via phase separation during spin-casting. *Advanced Functional Materials*, in press, 2005.

[26] JA Menendez, MD Barbacid, S Montero, E Sevilla, E Escrich, M Solanas, H Cortes-Funes, and R Colomer. Effects of gamma-linolenic acid and oleic acid on paclitaxel cytotoxicity in human breast cancer cells. *European Journal of Cancer*, 37(3):402–413, 2001.

[27] Peter L. Hagelstein, Stephen D. Senturia, and Terry P. Orlando. *Introductory applied quantum and statistical mechanics*. Wiley-Interscience, Hoboken, N.J., 2004.

[28] Robert Martin Eisberg and Robert Resnick. *Quantum physics of atoms, molecules, solids, nuclei, and particles.* Wiley, New York, 2nd edition, 1985.

[29] Charles Kittel. *Introduction to solid state physics.* Wiley, New York, 7th edition, 1996.

[30] J. M. Pietryga, R. D. Schaller, D. Werder, M. H. Stewart, V. I. Klimov, and J. A. Hollingsworth. Pushing the band gap envelope: Mid-infrared emitting colloidal pbse quantum dots. *Journal of the American Chemical Society*, 126(38):2, 2004.

[31] G Binnig, CF Quate, and C Gerber. Atomic force microscope. *Physical Review Letters*, 56(9):930–933, 1986.

[32] Stanley Wolf and Richard N. Tauber. *Silicon processing for the VLSI era.* Lattice Press, Sunset Beach, Calif., 1986.

[33] J. Aizenberg, A. J. Black, and G. M. Whitesides. Control of crystal nucleation by patterned self-assembled monolayers. *Nature*, 398(6727):3, 1999.

[34] S. Coe-Sullivan. *Private Communication*, 2004.

[35] L. Kim. *Private Communication*, 2005.

[36] Y. Hirose, A. Kahn, V. Aristov, P. Soukiassian, V. Bulovic, and S. R. Forrest. Chemistry and electronic properties of metal-organic semiconductor interfaces: Al, ti, in, sn, ag, and au on ptcda. *Physical review. B, Condensed matter*, 54(19):11, 1996.

[37] AJ Fernandes and DM Kane. Enhanced laser cleaning via direct line beam irradiation. *Applied Physics A - Material Science & Processing*, 79(4-6):735–738, 2004.

[38] F. Beaudoin, M. Meunier, M. Simard-Normandin, and D. Landheer. Excimer laser cleaning of silicon wafer backside metallic particles. *Journal of vacuum science & technology. A, Vacuum, surfaces, and films: an official journal of the American Vacuum Society*, 16(3 2):4, 1998.

[39] N Arnold, G Schrems, and D Bauerle. Ablative thresholds in laser cleaning of substrates from particulates. *Applied Physics A - Material Science & Processing*, 79(4-6):729–734, 2004.

[40] Ramkumar Krishnan, Hung Q Nguyen, Carl V Thompson, Wee K Choi, and Yong L Foo. Wafer-level ordered arrays of aligned carbon nanotubes with controlled size and spacing on silicon. *Nanotechnology*, 16(6):841–845, 2005.

[41] S. Fournier-Bidoz, V. Kitaev, D. Routkevitch, I. Manners, and G. A. Ozin. Highly ordered nanosphere imprinted nanochannel alumina (nina). *Advanced materials*, 16(23):3, 2004.

[42] Shoso Shingubara. Fabrication of nanomaterials using porous alumina templates. *Journal of Nanoparticle Research*, 5(1-2):14, 2003.

[43] H. Asoh, K. Nishio, M. Nakao, T. Tamamura, and H. Masuda. Conditions for fabrication of ideally ordered anodic porous alumina using pretextured al. *Journal of the Electrochemical Society*, 148(4):B152, 2001.

[44] R. Krishnan. *Private Communication*, 2005.

[45] H Masuda and K Fukuda. Ordered metal nanohole arrays made by a two-step replication of honeycomb structures of anodic alumina. *Science*, 268(5216):1466–1468, 1995.

[46] D. Routkevitch, A. A. Tager, J. Haruyama, D. Almawlawi, M. Moskovits, and J. M. Xu. Nonlithographic nano-wire arrays: Fabrication, physics, and device applications. *IEEE transactions on electron devices*, 43(10):13, 1996.

[47] Jong-Sung Yu, Jeong Yeon Kim, Seungho Lee, Jeremiah K. N. Mbindyo, Benjamin R. Martin, and Thomas E. Mallouk. Template synthesis of polymer-insulated colloidal gold nanowires with reactive ends. *Chemical Communications*, 2000(24):2445–2446, 2000.

[48] K Cooper, J Cooper, J Groschopf, J Flake, Y Solomentsev, and J Farkas. Effects of particle concentration on chemical mechanical planarization. *Electrochemical and Solid State Letters*, 5(12):G109–G112, 2002.

[49] P. A. Lewis, H. Ahmed, and T. Sato. Silicon nanopillars formed with gold colloidal particle masking. *Journal of vacuum science & technology*, 16(6):4, 1998.

[50] T. Thurn-Albrecht, R. Steiner, J. DeRouchey, C. M. Stafford, E. Huang, M. Bal, M. Tuominen, C. J. Hawker, and T. R. Russell. Nanoscopic templates from oriented block copolymer films. *Advanced materials*, 12(11):4, 2000.

[51] Amanda L. Giermann and Carl V. Thompson. Solid-state dewetting for ordered arrays of crystallographically oriented metal particles. *Applied physics letters*, 86(12):1, 2005.

[52] Xiao-Mei Zhao, Younan Xia, and George M. Whitesides. Soft lithographic methods for nano-fabrication. *Journal of Materials Chemistry*, 7(7):1069, 1997.

[53] C. Madigan. *Private Communication*, 2005.